

Contrasting lightning projection using the lightning potential index adapted in a convection-permitting regional climate model

Erwan Brisson (✉ erwan.brisson@gmail.com)

Goethe-Universität Frankfurt am Main Fachbereich 11 Geowissenschaften Geographie
<https://orcid.org/0000-0003-2558-2556>

Ulrich Blahak

Deutscher Wetterdienst

Philippe Lucas-Picher

CNRM GMGEC: Centre National de Recherches Meteorologiques Groupe de Meteorologie de Grande Echelle et Climat

Christopher Purr

Goethe-Universität Frankfurt am Main Fachbereich 11 Geowissenschaften Geographie

Bodo Ahrens

Goethe-Universität Frankfurt am Main Fachbereich 11 Geowissenschaften Geographie

Research Article

Keywords: Convection-permitting climate model, COSMO-CLM, Lightning, Microphysics, Extremes

Posted Date: March 26th, 2021

DOI: <https://doi.org/10.21203/rs.3.rs-339754/v1>

License:  This work is licensed under a Creative Commons Attribution 4.0 International License.

[Read Full License](#)

1 **Contrasting lightning projection using the lightning**
2 **potential index adapted in a convection-permitting**
3 **regional climate model**

4 **Erwan Brisson · Ulrich Blahak · Philippe**

5 **Lucas-Picher · Christopher Purr · Bodo**

6 **Ahrens**

7 the date of receipt and acceptance should be inserted later

8 **Abstract** Lightning climate change projections show large uncertainties caused by
9 limited empirical knowledge and strong assumptions inherent to coarse-grid cli-
10 mate modeling. This study addresses the latter issue by implementing and applying

E. Brisson

Goethe University Frankfurt, Frankfurt, Germany

Centre National de Recherche Meteorologique, CNRS, Toulouse, France

E-mail: erwan.brisson@gmail.com

P. Lucas-Picher

Centre National de Recherche Meteorologique, CNRS, Toulouse, France

U. Blahak

Deutscher Wetterdienst (DWD), Offenbach, Germany

B. Ahrens

Goethe University Frankfurt, Frankfurt, Germany

C. Purr

Goethe University Frankfurt, Frankfurt, Germany

the lightning potential index parameterization (LPI) into a fine-grid convection-permitting regional climate model (CPM). This setup takes advantage of the explicit representation of deep convection in CPMs and allows for process-oriented LPI inputs such as vertical velocity within convective cells and coexistence of microphysical hydrometeor types, which are known to contribute to charge separation mechanisms. The LPI output is compared to output from a simpler flash rate parameterization, namely the CAPE \times PREC parameterization, applied in a non-CPM on a coarser grid. The LPI's implementation into the regional climate model COSMO-CLM successfully reproduces the observed lightning climatology, including its latitudinal gradient, its daily and hourly probability distributions, and its diurnal and annual cycles. Besides, the simulated temperature dependence of lightning reflects the observed dependency. The LPI outperforms the CAPE \times PREC parameterization in all applied diagnostics. Based on this satisfactory evaluation, we used the LPI to a climate change projection under the RCP8.5 scenario. For the domain under investigation centered over Germany, the LPI projects a decrease of 4.8% in flash rate by the end of the century, in opposition to a projected increase of 17.4% as projected using the CAPE \times PREC parameterization. The future decrease of LPI occurs mostly during the summer afternoons and is related to (i) a change in convection occurrence and (ii) changes in the microphysical mixing. The two parameterizations differ because of different convection occurrences in the CPM and non-CPM and because of changes in the microphysical mixing, which is only represented in the LPI lightning parameterization.

Keywords Convection-permitting climate model · COSMO-CLM · Lightning · Microphysics · Extremes

1 Introduction

Current lightning climate simulations mainly rely on parameterizations, which relate climate model output to observed lightning (Clark et al., 2017), but rarely closely reflect the physical mechanisms leading to lightning. Indeed the complexity, the spatio-temporal scales, and the diversity of mechanisms related to lightning flashes do not allow global climate models for its explicit representation. As an example, the mechanism dominating thunderstorm electrification is known as the non-inductive charging mechanism (Reynolds et al., 1957; Takahashi, 1978; Saunders, 1993; Saunders and Peck, 1998; Latham et al., 2007). It implies electric charge separation through rebounding collision between small ice crystals growing by water vapor diffusion and graupel pellets growing by accretion of supercooled water droplets (Yair, 2008). The sign and the magnitude of the charge exchanged between ice crystals and graupel pellets depend on many parameters (e.g., temperature, cloud water content, rime accretion rate, etc. - Jayaratne et al. (1983); Saunders (2008)). Once the charge is exchanged, the ice particles are dispersed in the clouds through gravitational processes, with heavy graupel pellets moving downward relatively to the ice crystals (Williams, 1988; Houze, 2014). On the macro scale, the cloud will, therefore, be characterized by multiple large cloud layers with homogeneous polarities (Stolzenburg et al., 1998a,b,c).

The non-inductive process is mainly occurring in areas with convective activity. Therefore, many parametrizations relate the occurrence, and sometimes the intensity, of the convective activity to derive flash densities (Finney et al., 2016). An example of such a parameterization is the convective available potential energy times the precipitation rates ($CAPE \times PREC$) used to derive the lightning

59 flash rate. With these simple and easily accessible variables, it is possible to obtain
60 both the location where flashes are likely to occur, but also the intensity of the
61 flash activity as high CAPE and high precipitation rate indicate high convective
62 activity. Over the contiguous United States, Romps et al. (2014) found that this
63 parameterization explains 77% of the temporal variance in the lightning flash rate.
64 Another approach commonly used for parameterizing lightning in climate models
65 is based on the observed relationship between the cloud top height (CTH) and
66 the flash rates (Price and Rind, 1992), the cloud height being a good indicator
67 for the occurrence and the intensity of convective activity. While such a relation-
68 ship compares well to current observations, it is unknown whether it will hold in
69 a different climate. For example, while CTH is expected to increase in a warmer
70 climate, so does the cloud base height (Chepfer et al., 2014), which may result in
71 constant cloud depth. Yoshida et al. (2009) used cold cloud height to tackle this
72 issue, but all these parameterizations are still highly dependent on the empirical
73 relationship and may be far away from representing the electrification process,
74 notably the non-inductive one.

75 Closer to the theoretical mechanism, some more advanced lightning param-
76 eterizations have been implemented by introducing variables accounting for the
77 microscale processes. For example, the ice mass flux scheme (Finney et al., 2014,
78 2018) uses the upward cloud ice flux at 440 hPa. Although the variables selected
79 in more complex parameterizations are uncommon GCM output, they allow for
80 clear improvements both spatially and temporally, over parameterization essen-
81 tially based on the convective activity (Finney et al., 2014). Moreover, while most
82 of the convective activity-based parameterizations shows an increase in lightning
83 flashes in a warmer climate (e.g., $12 \pm 5\%$ per $^{\circ}\text{C}$ increase for $\text{CAPE} \times \text{PREC}$

84 (Romps et al., 2014) or from 7 to 13% per °C increase for CTH (Krause et al.,
85 2014; Clark et al., 2017)), the first flash rate climate projection based on the ice
86 mass flux scheme parameterization (Finney et al., 2018) show decreasing lightning
87 toward the end of the century following the RCP 8.5. These results are promising
88 for the climate community, but the ice mass flux scheme still suffers from signif-
89 icant inadequacies (Finney et al., 2018). First, accounting for the ice flux on a
90 single level is still far from representing the non-inductive charging mechanism.
91 Second, the variables from which the ice flux scheme is based on, are still strongly
92 parameterized in current GCM.

93 For example, the variability of hydrometeors or that of convective up/down-
94 drafts have scales that are currently far from being explicitly represented in global
95 climate models (Prein et al., 2015). The updraft is particularly critical as it con-
96 ditions hydrometeors' transport, the growth of graupel through riming, and the
97 chances for collisions between ice crystals and graupel pellets (Houze, 1993). Mi-
98 crophysical processes will remain parameterized in the next generation of global
99 climate projections. Recently, Lopez (2016) developed a new lightning parameter-
100 ization for the global convection-parameterizing NWP model IFS of ECMWF. It
101 employs diagnosed vertical profiles of graupel and supercooled liquid from within
102 the convection parameterization and CAPE to form an estimator for the flash
103 rate. While physically more sound, its possible performance in current coarse-grid
104 GCMs is not clear.

105 However, the first convection-permitting projections produced by regional cli-
106 mate models are now available (Prein et al., 2015). These models show realistic
107 representations of convective processes in general (Leutwyler et al., 2017). On the
108 hourly and sub-hourly scales, convection-permitting models (CPM) improved the

109 representation of spatial precipitation patterns and extremes values (Prein et al.,
110 2013; Brisson et al., 2016, 2018). The representation of convective clouds also
111 shows improved features (Brisson et al., 2016; Keller et al., 2016). Interestingly,
112 the sensitivity of convective related variables derived from CPM to global warming
113 does not always match that derived from coarser climate models, as observed by,
114 e.g., Kendon et al. (2014); Vanden Broucke et al. (2019); Helsen et al. (2020).

115 Besides, the improved representation of convective processes allows for more
116 complex parameterizations (Fierro et al., 2013). In McCaul et al. (2009), the flash
117 rate is estimated based on the resolved upward flux of graupel in the mixed-
118 phased region at $-15^{\circ}C$ and the integration of solid hydrometeors over the full
119 storm depth.. This parameterization is related to that established latter in Finney
120 et al. (2014) but fits closely to the non-inductive process as it focuses on graupel
121 and not anymore on the full ice content. Furthermore, it is applied at a specific
122 temperature level instead of a pressure one. One step further into the complexity is
123 the lightning potential index (LPI). The LPI accounts not only for the presence of
124 solid hydrometeors but also for the presence of both solid (with a stress on graupel)
125 and supercooled liquid hydrometeors. Besides, it uses all atmospheric levels ranging
126 from $-20^{\circ}C$ to $0^{\circ}C$. Proposed by Yair et al. (2010), this parameterization was
127 applied to several case studies with CPMs. The LPI shows a high correlation
128 with observed lightning (Yair et al., 2010; Lynn and Yair, 2010; Lagasio et al.,
129 2017). To the authors' knowledge, the output of such parameterization has only
130 been applied to short periods for numerical weather prediction purposes. With
131 the rise of multi-decadal CPM simulations, such parameterization could now be
132 applied on a climate time scale. According to Kendon et al. (2016), the climate

133 community expects an improved representation of lightning with CPMs and that
134 further developments/research are needed in that direction.

135 This study aims in this direction. While many paths are open, we choose to
136 start with the following questions: Can more complex parameterizations such as
137 the LPI provide a realistic representation of lightning? What is the added value
138 of these parameterizations applied to CPMs when compared to simpler param-
139 eterization used in non-CPMs? Do the projections of flash rates as represented
140 by such complex parameterizations differ from that of simpler non-CPM parame-
141 terizations? To provide elements of answers to these questions, the lightning po-
142 tential index (LPI) will be implemented and applied in a CPM and compared to
143 the CAPE \times PREC parameterization applied to a non-CPM. The models and
144 their parameterizations are detailed in the methods section, together with an ob-
145 servational dataset. Such an indirect comparison of a CPM with one lightning
146 parameterization and a non-CPM using another might appear to be not ideal at
147 first glance. The fact is that LPI is not easy to implement in a non-CPM (lack
148 of explicit convective updrafts, supercooled liquid, and graupel), while CAPE \times
149 PREC has severe problems in a CPM (CAPE-removal by explicit convection leads
150 to a null CAPE where there is PREC and vice versa). The validation of the pa-
151 rameterizations against observations and an investigation on flash rate projections
152 are described in the result section. The added value of a parameterization like the
153 LPI compared to current GCM parameterizations is discussed but is not the main
154 focus of this paper. Finally, the conclusion provides elements of answers to the
155 research questions listed above.

156 2 Methods

157 2.1 Model setup and lightning parameterizations

158 All simulations investigated in this study were performed using the Consortium
159 for Small-scale Modelling in climate mode (COSMO-CLM) model. The COSMO-
160 CLM model is a non-hydrostatic limited-area climate model, based on the COSMO
161 model (Steppeler et al., 2003; Doms et al., 2011), a model designed by the Deutsche
162 Wetterdienst (DWD) for operational weather predictions. The climate limited-area
163 modeling (CLM) community adapted this model to perform climate projections
164 (Böhm et al., 2006; Rockel et al., 2008). We used the version COSMO5.0 clm7.

165 In all COSMO-CLM simulations performed in this study, we use the 5th order
166 Runge-Kutta split-explicit time-stepping scheme (Wicker and Skamarock 2002),
167 the lower boundary fluxes provided by the TERRA model (Doms et al., 2011), the
168 radiative scheme after Ritter and Geleyn (1992), and the one-moment microphysi-
169 cal scheme (Steppeler et al., 2003; Doms et al., 2011). Besides, as recommended by
170 Brisson et al. (2016), in the CPM, the one-moment microphysical scheme predicts
171 the mass evolution of graupel, in addition to the four standard hydrometeor types
172 (i.e., cloud droplets, raindrops, cloud ice, snow). Such configuration is close to the
173 operational convection-allowing limited area configuration COSMO-DE of DWD
174 (Baldauf et al., 2011). Finally, in the CPM parent nest, the wind’s horizontal com-
175 ponents, together with the temperature, are spectrally nudged to reduce boundary
176 effect.

177 The finest nest is centered over central Germany (Fig. 1) at a resolution of
178 0.025° (~ 3 km). A double-step one-way nesting strategy is applied to reach this
179 resolution. The global fields, i.e., ERA-Interim for the hindcast simulation (1981-

180 2015), and the EC-Earth ensemble member r12i1p1 for both the historical period
181 (1975-2005) and the RCP8.5 projection (2071-2100), are used to drive a 0.22° (\sim
182 25 km) grid mesh COSMO-CLM simulation over a limited-area centered over Eu-
183 rope. In a second step, the resulting hourly outputs of this simulation are used to
184 drive the 0.025° COSMO-CLM simulation. While the 0.22° simulations are per-
185 formed with a parameterization of deep and shallow convection following Tiedtke
186 (1989), in the 0.025° simulations, only the shallow (non-precipitating) part of that
187 convection parameterization is activated, allowing for the explicit simulation of
188 convective cells with their associated strong up- and downdrafts and microphysi-
189 cal mixed-phase precipitation formation processes.

190 In the innermost convection-allowing COSMO domain, we adopt the LPI pa-
191 rameterization of Lynn and Yair (2010) and Yair et al. (2010) as described in
192 Section 2.1.1. This parameterization uses the local microphysical conditions for
193 charge separation in updrafts as a necessary condition for lightning, in a relatively
194 simple and computationally cheap way.

195 There are more accurate schemes in the literature, which explicitly predict
196 charged hydrometeors, the dynamics of atmospheric charge distribution, and as-
197 sociated lightning discharge when the electric potential between any two points in
198 space rises above a threshold, e.g., Barthe and Pinty (2007); Barthe et al. (2012).
199 However, such schemes would have been much too computationally expensive for
200 the present study.

201 *2.1.1 The Lightning potential index (LPI) parameterization*

202 This parameterization is based on the LPI parameterization proposed by Lynn
203 and Yair (2010) and Yair et al. (2010) was adapted and implemented into the

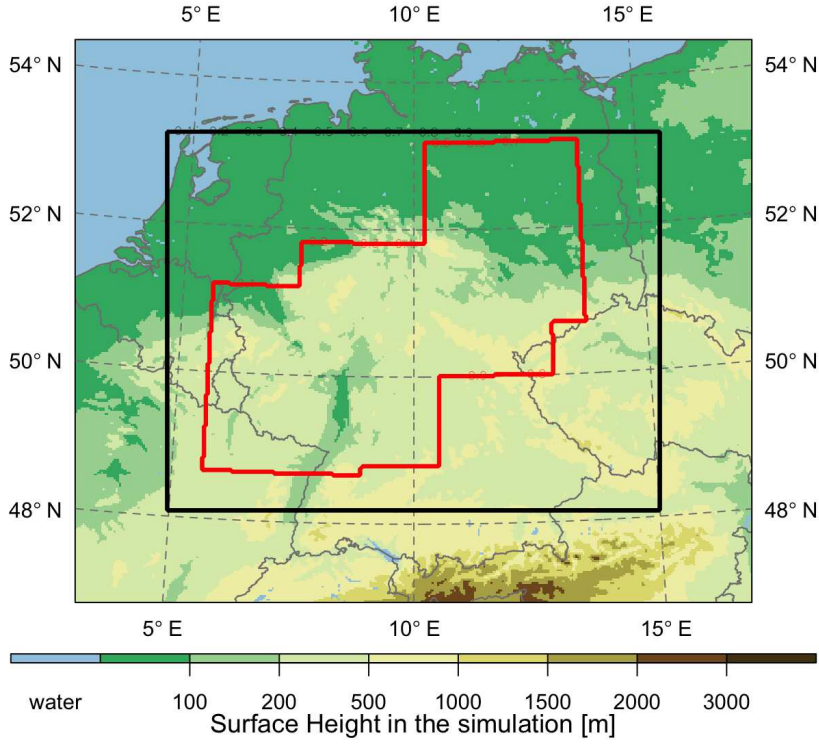


Fig. 1: Domain of the 0.025° simulation. The red polygon indicates the area where observations are available and, therefore, also the evaluation domain. The black rectangle shows the domain used for the analyses other than the evaluation.

204 COSMO model by one of the authors (U. Blahak) in 2014. Subsequently, it has
 205 been evaluated in an NWP context by Sokol and Minarova (2020) and found to
 206 be a useful COSMO diagnostic for lightning forecasting. The LPI is defined as

$$LPI = f_1 f_2 \frac{1}{H_{-20^\circ C} - H_{0^\circ C}} \int_{H_{0^\circ C}}^{H_{-20^\circ C}} \epsilon w^2 g_{(w)} dz \quad (1)$$

207 and represents the kinetic energy of the updraft - derived from the vertical wind
 208 speed - scaled by the potential for charge separation inherent to the microphysical

209 mixing. The latter is given by the function

$$\epsilon = 2 \frac{\sqrt{q_L q_F}}{q_L + q_F} \quad (2)$$

210 with

$$q_L = q_c + q_r \quad (3)$$

211

$$q_F = q_g \left(\frac{\sqrt{q_i q_g}}{q_i + q_g} + \frac{\sqrt{q_s q_g}}{q_s + q_g} \right) \quad (4)$$

212 where q_c , q_r , q_i , q_s and q_g are the mixing ratios of cloud water, rain water, cloud
 213 ice, snow and graupel, respectively. q_L is the sum of the liquid species, while q_F
 214 represents (weighted) contributions of the frozen hydrometeors. In essence, ϵ is the
 215 ratio of the geometric to the arithmetic mean of two quantities. It also appears
 216 twice in q_F .

217 ϵ takes a value of 1 when the liquid water and the solid hydrometeors masses
 218 are equal to 0 when all the water is in the same phase (e.g., solid or liquid).
 219 These values are vertically averaged over the primary charging zone, ranging from
 220 $0^\circ C$ to $-20^\circ C$. Moreover, non-zero values can only be attained if – besides the
 221 supercooled liquid water – graupel, and a second non-rimed species (in our case
 222 q_i or q_s), are present at the same time, representing the non-inductive charge
 223 separation mechanism.

224 In addition, the boolean function

$$g(w) = \left\{ \begin{array}{ll} 1 & \text{if } w \geq 0.5 \text{ m/s} \\ 0 & \text{else} \end{array} \right\} \quad (5)$$

225 restricts the vertical averaging to grid boxes having updrafts above a threshold of
 226 0.5 m/s (Lynn and Yair, 2010).

227 To prevent spurious and unrealistic LPI signals in areas of weak, isolated up-
 228 draft columns as well as in deep orographic gravity wave clouds (lenticularis), two

229 additional filter functions f_1 and f_2 are applied. These functions are not directly
230 related to the parameterized physical mechanisms of charge separation in the LPI
231 and are briefly described in Appendices A and B.

232 The LPI has to be calibrated by observations to be an estimator for the flash
233 rate.

234 *2.1.2 The CAPE \times PREC parameterization*

235 The convection-permitting model's performance using LPI in representing light-
236 ning is compared to that of the coarser 0.22° model. Applying the LPI parameteri-
237 zation is impossible in this non-CPM due to the lack of strong updrafts and graupel
238 hydrometeors. Another parameterization, namely the CAPE \times PREC product as
239 a flash rate estimator, is applied here. This parameterization performed well in
240 representing flash rates over the contiguous United States (Romps et al., 2014)
241 and is the only parameterization which could be derived from the available output
242 of our 0.22° simulation.

243 As mentioned before, please note that the CAPE \times PREC parameterization
244 can hardly be directly applied to a CPM, as CAPE is rapidly depleted at locations
245 of convective cells by latent heat release in moist adiabatic updrafts and evapora-
246 tive cooling in precipitation below the cloud base. Therefore, a direct comparison
247 of both parameterizations in the CPM framework is rarely applied in this study.

248 To a lesser degree, this depletion also happens in the Tiedtke parameterization
249 of deep convection. Precipitation is produced simultaneously as the instability
250 is gradually removed from the atmosphere leading to a lower CAPE in the grid
251 column where convective precipitation is produced. Thus, multiplying the hourly
252 CAPE with the hourly accumulated precipitation as output by the model results in

253 relatively low CAPE \times PREC values. To tackle this issue, the CAPE at time t was
254 multiplied by the precipitation accumulated from time t to $t+1$ hour. This method
255 was selected as it shows the closest fit to observed flash rates when compared to
256 other methods (e.g., using daily average, using precipitation accumulated from
257 time $t - 30$ min to $t + 30$ min).

258 Similarly, The CAPE \times PREC values have to be calibrated by observations to
259 be an estimator for the flash rate.

260 2.2 Validation dataset

261 The lightning observations were extracted from the BLIDS dataset (Blitz Infor-
262 mation Dienst Siemens (2019)). The raw spatial resolution of the BLIDS data
263 ranges from 200 m to 700 m, and the temporal resolution is 1 ms. The BLIDS net-
264 work measures lightning since 1992 and improved several times since then (Schulz
265 and Diendorfer, 2004). Besides, the observation sensors were upgraded in 1999, re-
266 sulting in an improved detection of strokes, especially intra-clouds ones (Schulz and
267 Diendorfer, 2004). This upgrade led to temporal inhomogeneities when integrating
268 over the full period (i.e., before and after the upgrade of the sensors). To avoid
269 these inhomogeneities, the model simulations are evaluated for the period 2000 to
270 2013 only. Besides, the evaluation domain was restricted to areas for which the
271 German regional agencies TLUG (Thüringen), LAU (Sachsen-Anhalt), HLNUG
272 (Hessen), and FAWF (Rheinland-Pfalz) provided us with the BLIDS dataset over
273 each corresponding region.

274 2.3 Analysis method

275 2.3.1 Adjustment of parameterizations output

276 The observations and the output of lightning parameterizations do not match
 277 directly in terms of units, spatial and temporal scales. This mismatch prevents the
 278 comparison of the parameterization output directly with the observations. This
 279 issue is tackled by remapping the observations to the CPM grid using a conserva-
 280 tive remapping. Besides, the flashes are grouped into 15-minute bins for the LPI
 281 parameterization and into hourly bins for the CAPE \times PREC parameterization
 282 by deriving the number of flashes occurring during a given time interval (i.e., ± 7.5
 283 minutes for the LPI, which was output every 15 minutes and ± 30 minutes for the
 284 CAPE \times PREC, which was output every hour).

285 Finally, we converted the parameterization's output to flash rates in a two-step
 286 procedure. First, the lowest values of the parameterization's output are set to 0,
 287 so that the occurrence of values above zero is adjusted to that of the observation.
 288 Second, a simple linear model is built that relates the observed flash rates to
 289 the parameterization output. The use of a linear adjustment is motivated by the
 290 high correlation found in Romps et al. (2014) suggesting a linear relation for the
 291 CAPE \times PREC parameterization. Besides, such linear models are not likely to result
 292 in overfitting with only two parameters to calibrate, having a large sample size.
 293 The adjusted values are therefore derived based on the following equations:

$$\begin{cases} X_{adj} = aX + b & \text{if } X \geq c \\ X_{adj} = 0 & \text{else} \end{cases} \quad (6)$$

294 where X is the parameterization output, and a , b , and c are three coefficients,
 295 which were calibrated using the accumulated observed flashes rates for each grid-

296 point and the parameterization output from the ERA-Interim driven simulations.
 297 For the period 2000-2013, $a = 0.405$, $b = -0.073$ and, $c = 0.33$ for the LPI pa-
 298 rameterization and $a = 0.000172$, $b = 0.0118$ and, $c = 15.85$ for the CAPE×PREC
 299 parameterization provide the best adjustments (i.e., the lowest root mean square
 300 error between the observed and simulated flash rate probability density). In addi-
 301 tion, note that the adjustment does not alter the climate change signal described
 302 in Section 3.2. The latter is of similar amplitude for both the LPI and the LPI_{adj} .

303 As defined above, the X_{adj} provides a number of flashes per grid-cell. To avoid
 304 a dependency of the flash rate to cell size, two strategies were adopted. First, the
 305 unit flash rate per km^2 per time period is adopted through all this manuscript.
 306 Second, the evaluation was mostly performed using spatial averaging over the
 307 full domain. While this may limit the analysis of high local values (e.g., flashes
 308 from local storms), it strengthens the analysis' robustness. Besides, it allows for a
 309 fair comparison between the two parameterizations, which are applied to different
 310 spatial resolutions.

311 The X_{adj} is written as X unless specified otherwise in this manuscript to ease
 312 the reading.

313 2.3.2 Skill scores

314 The performance of the model is evaluated using the mean square skill score
 315 (MSSS, Murphy (1988)), which is derived as

$$MSSS = 1 - \frac{\sum_{i=1}^n w_i (s_i - o_i)^2}{\sum_{i=1}^n w_i (\bar{o} - o_i)^2} \quad (7)$$

316 where s and o respectively represent the simulation and observational datasets, n
 317 the sample size, and w the weighting function. In this manuscript, the weighting

function is set to one unless specified otherwise. The MSSS is equal to 1 when the simulation is identical to the observation and is greater than 0 when the simulation is more realistic than the observed climatology (\bar{o}).

In addition, the probability density functions (PDFs) are evaluated using the Perkins skill score (PSS, Perkins et al., 2007), which measures the common area between two PDFs by calculating their cumulative minimum for each group of binned values,

$$PSS = \sum_{i=1}^n \min(Z_s(i), Z_o(i)), \quad (8)$$

where i is the bin index, n is the total number of bins, and $Z_s(i)$ and $Z_o(i)$ are the simulation- and observation-probability masses, respectively. Two PDFs are identical when the PSS is equal to 1. Besides, Perkins et al. (2007) suggests that two PDFs differ significantly from each other when their PSS is lower than ~ 0.7 .

2.3.3 Uncertainty and significance

The flash rate uncertainty is estimated through bootstrapping with replacement. This bootstrapping is performed by randomly selecting blocks from the original time series to create a new time series of similar length, hereafter referred to as bootstrap. Blocks of one month are selected to keep the temporal dependency of the data. Also, an equal number of each month is selected in each bootstrap (e.g., n January, n February, n March, etc.), to account for the seasonal variability. The uncertainty is derived using 100 bootstraps by taking the range between the 2.5th and 97.5th percentiles of the studied quantity.

These bootstraps are also used to assess whether two simulations significantly differ from each other. For each of the two sets of 100 bootstraps, the studied

340 quantity is derived (e.g., the average value for a given month). The differences
 341 between all pairs from these two sets are then computed, resulting in 10000 values.
 342 A significant change at the l level is detected when the $l/2$ and the $100 - l/2$
 343 percentiles of these 10000 values are respectively greater or smaller than 0 such as

$$0 \notin [\textit{percentile}_{l/2}, \textit{percentile}_{100-l/2}] \quad (9)$$

344 **3 Results**

345 **3.1 Evaluation**

346 Figure 2 compares the probability densities of the modeled daily lightning flash
 347 rate computed from the two parameterizations with the observations. Both param-
 348 eterizations fairly reproduce the observed hourly and daily flash rate probability
 349 densities over the domain where observations are available. Still, the LPI outper-
 350 forms the CAPE \times PREC resulting in PSSs of respectively 0.93 and 0.77 for the
 351 hourly timescale and 0.84 and 0.73 for the daily timescale.

352 The observed flash rate is spatially heterogeneous (Fig. 3a). High flash rates
 353 are observed along the Rhine valley ($\sim 9^\circ E$, ~ 49 to $52^\circ N$), as well as an area over
 354 near the southeastern corner of the evaluation domain while lower flash rates are
 355 found in the north and between 10 and $12^\circ E$. A negative north to south gradient
 356 is also observed. The small scale spatial variability is poorly reproduced by both
 357 parameterizations ($MSSS$ of -0.14 for the LPI and -0.25 for the CAPE \times PREC).
 358 However, the north to south gradient is well captured by LPI with an $MSSS$ of
 359 0.61 (Fig. 4). The CAPE \times PREC parameterization produces a north to south
 360 gradient that is too steep, resulting in a bias larger than the observed climatology,
 361 as indicated by the $MSSS$ of -1.66.

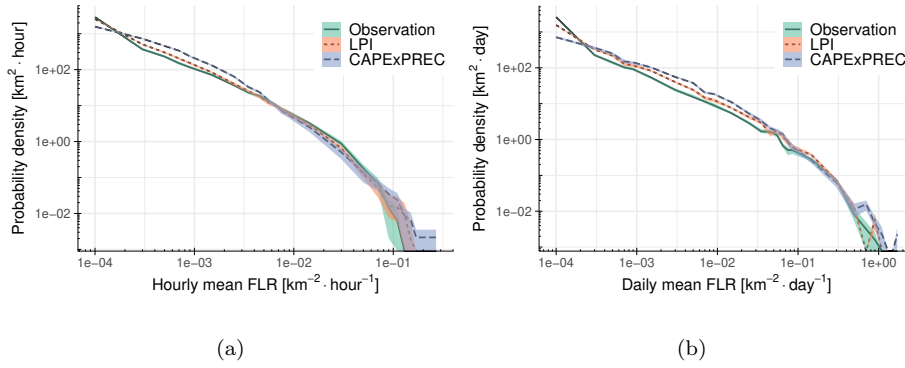


Fig. 2: Probability densities of the domain average (a) hourly and (b) daily flash rates as observed (solid line), as represented by the LPI (short-dashed line), and by the $CAPE \times PREC$ (long-dashed line) parameterizations. The shaded areas represent the uncertainty derived through the bootstrapping technique with replacement introduced in the method section.

362 One of the main challenges in non-CPM simulations is the representation of
 363 the convective activity's diurnal cycle. CPMs generally improve the representation
 364 of the diurnal cycle of convective precipitation (Prein et al., 2015). Here, the
 365 diurnal cycle of the LPI follows closely that of the observation with a minimum
 366 hourly flash rates in the morning and a maximum in the mid-afternoon (Fig. 5 -
 367 $MSSS = 0.95$) as opposed to the $CAPE \times PREC$ ($MSSS = 0.41$). Indeed, the
 368 $CAPE \times PREC$ diurnal cycle shows a flatter mid-afternoon peak with too early
 369 occurrence of flash rates. The LPI largely corrects these biases with an improved
 370 timing of the mid-afternoon peak that falls within the sampling uncertainty. The
 371 difference in performance between the two parameterizations is similar to that
 372 found for precipitation when comparing CPM and non-CPM (Ban et al., 2014;
 373 Brisson et al., 2016).

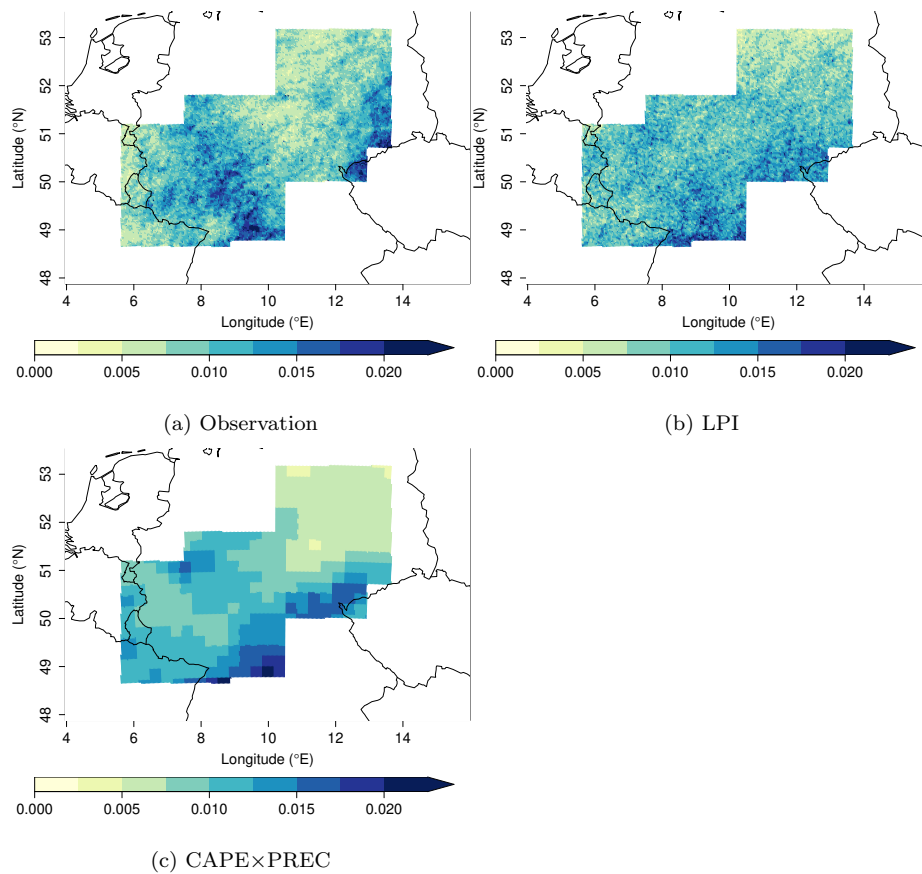


Fig. 3: Spatial distribution of daily averaged observed and modeled flash rate ($Flash\ m^{-2}\ hour^{-1}$) over the period 2000-2013.

374 The investigations described above focus on the flash rate parameterizations
 375 performance in modeling the current climatology of lightning. However, limited
 376 information is provided on the model's robustness to provide reliable flash rate
 377 climatologies for different climates. As an indication of robustness, we studied the
 378 scaling of flash rates with 2m temperature. As shown in Fig. 6 the temperature
 379 scaling of the observed flash rates can roughly be decomposed into three parts, each

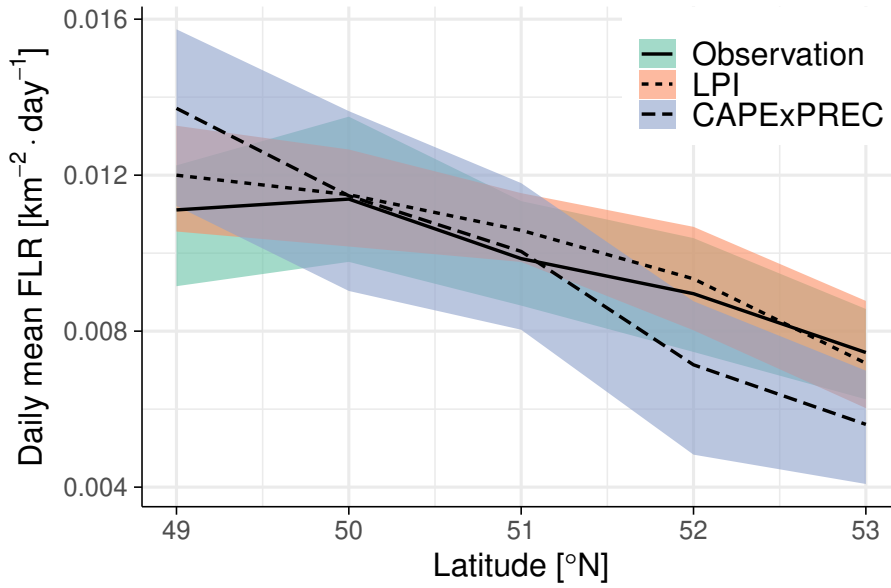


Fig. 4: Latitudinal dependence of the daily flash rates for the period 2000-2013. The solid line indicates the observation while the dashed lines show the parameterizations output (short dash for the LPI and long dash for the $\text{CAPE} \times \text{PREC}$). The shaded areas provide the sampling uncertainty derived from 100 bootstraps with replacement.

380 of them characterized by different exponential growth. The two related breakpoints
 381 occur at about 273 K and 294 K.

382 The LPI reproduces well the observed temperature scaling with similar expo-
 383 nential growth rates and breakpoints. However, the model overestimates the mean
 384 daily flash rate for the lowest temperatures and simulated a drop of flash rates for
 385 the highest temperature (higher than 301 K) as opposed to observed rates result-
 386 ing in an MSSS of 0.18. However, for these highest temperatures mean rates, the
 387 sampling size is small, as shown by the rug in Fig. 6. When weighting the MSSS

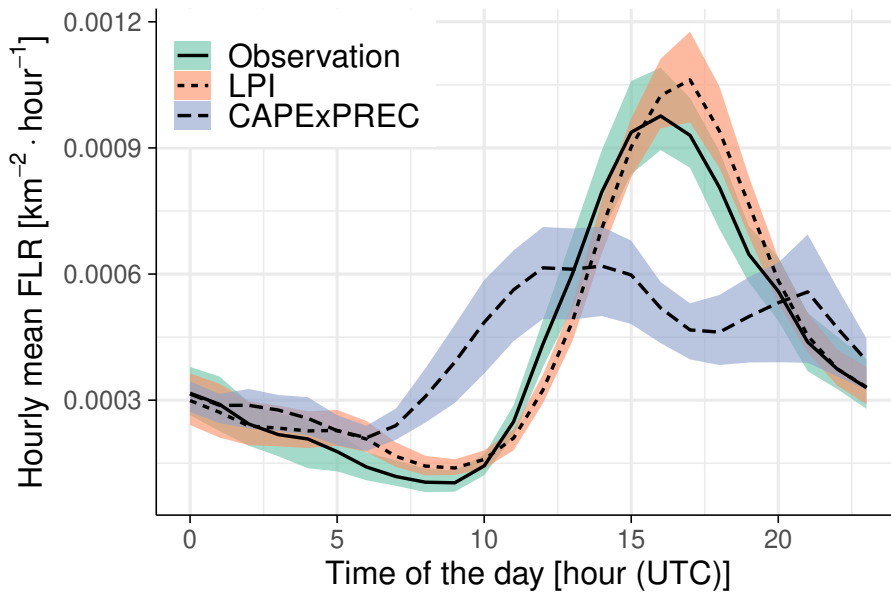


Fig. 5: Diurnal cycle of the hourly flash rate averaged over the evaluation domain and the period 2000-2013. The solid line indicates the observation, while the short-dashed line shows the LPI, and the long-dashed line shows the CAPE \times PREC diurnal cycles. The shaded areas provide the sampling uncertainty derived from 100 bootstraps with replacement.

388 with the sampling size of each bin, the MSSS increases to 0.83. A robust estimation
 389 of this possible misbehavior of the model would require a longer sampling period.

390 The CAPE \times PREC is worse at reproducing the observed temperature scaling
 391 than the LPI resulting in a weighted *MSSS* of 0.57. Still, CAPE \times PREC re-
 392 produces the tipping points and the general behavior of the temperature scaling.
 393 It should be noted that for the lowest and highest temperature bins, no flashes
 394 are produced by the CAPE \times PREC as opposed to the LPI. Generally, the ob-
 395 served frequency of days with flash occurrence (61.8%) is underestimated by both

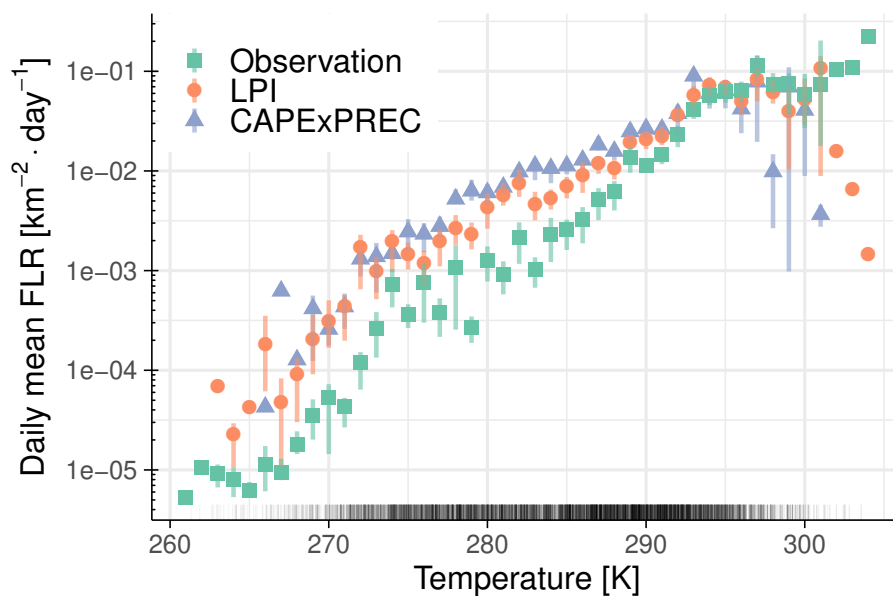


Fig. 6: The dependency of domain-averaged daily mean flash rates with daily temperature for the period 2000-2013. The observation (green squares) and the parameterizations (orange circle for the LPI and blue triangle for the CAPE \times PREC) are binned to temperature classes (i.e., one value per 1 K class). In addition, the corresponding bars provide the sampling uncertainty derived from 100 bootstraps with replacement when the sample size is larger than one. The rug at the bottom of the plot shows the simulated temperature values for the investigated period.

396 parameterization, with a larger underestimation for the CAPE \times PREC (43.5%)

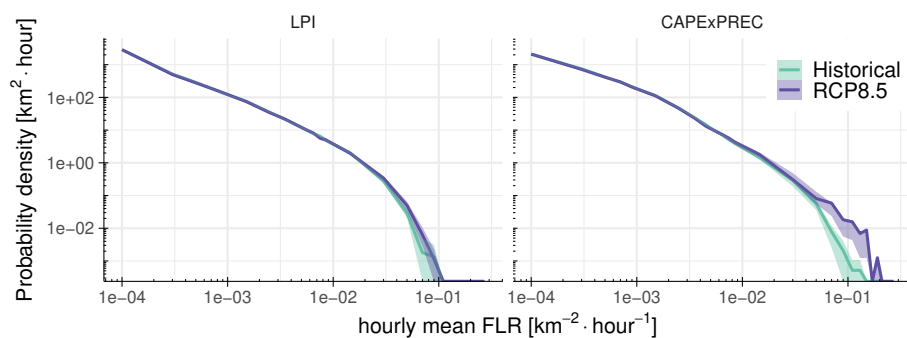
397 compared to that of the LPI 49.7%.

398 3.2 Climate projections

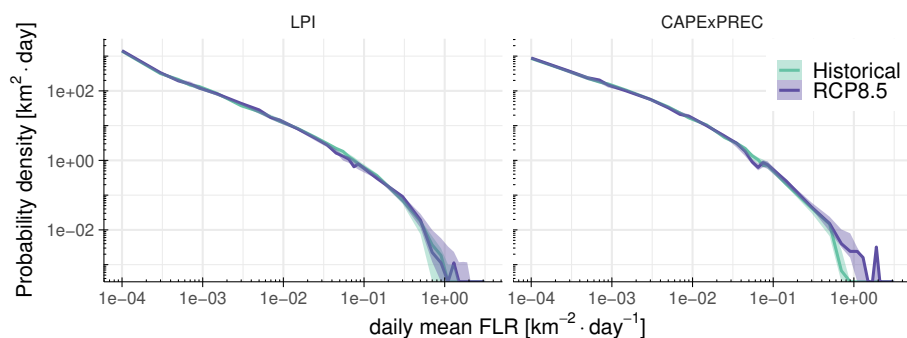
399 In this subsection, the evolution of the LPI and CAPE \times PREC parameterizations
400 with time under the RCP8.5 scenario is investigated. For this, the parameteriza-
401 tions are applied to COSMO-CLM driven by a historical (1975 to 2005) and a
402 future (RCP8.5 from 2071 to 2100) simulation. These simulations are used to
403 compare the climate change signal derived from the two parameterizations. While
404 the wording projection is used in the following section, these simulations do not
405 robustly indicate the evolution of lightning under a warmer climate for Germany,
406 which would require a larger simulation ensemble. When comparing the future with
407 the historical simulations, the two parameterizations show significantly different
408 changes at the 5% level with a decrease of -4.8% for the LPI and an increase of
409 $+17.4\%$ for the CAPE \times PREC. Note that the changes for both parameterizations
410 are independent of the latitude (Fig. S1 in supplemental material).

411 Fig. 7 shows that the climate change signal is not equally distributed on the
412 full range of flash rates. For most of the flash rate range, no climate change signal
413 is found. In contrast, the probability for high flash rates (i.e., flash rates above
414 the historical 95th percentiles) increases for both parameterizations on both the
415 daily and the hourly timescale. This increase is more substantial for the CAPE \times
416 PREC than for the LPI (e.g., the significant change at the 5% level of the 99.9th
417 percentiles is 64% for the CAPE \times PREC against 16% for the LPI).

418 As shown by the representation of the annual cycle (Fig. 8), the highest flash
419 rates are mostly occurring in summer. For both parameterizations, the highest
420 increase in flash rate is occurring in July. However, significant changes between
421 the historical and the RCP8.5 simulations are found for other months (May for



(a) Hourly distributions



(b) Daily distributions

Fig. 7: Probability densities of the domain average hourly flash rates (a) and domain average daily flash rates (b) as represented by the LPI and the $CAPE \times PREC$ parameterizations for EC-Earth driven simulations. The shaded areas represent the uncertainty and are derived through the bootstrapping technique with replacement introduced in the method section.

422 the LPI and January, February, October, and December for $CAPE \times PREC$). The
 423 changes are of opposite signs with a decrease for the LPI and an increase for the
 424 $CAPE \times PREC$.

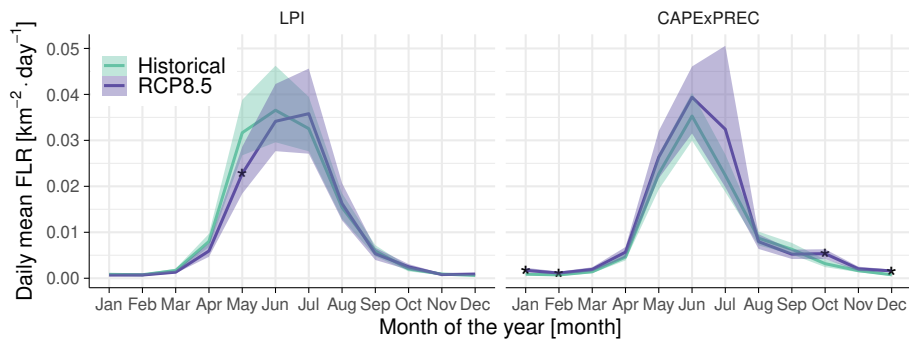


Fig. 8: Annual cycle of the daily mean flash rate for the COSMO EC-Earth historical (green) and the EC-Earth future driven simulations (purple). The shaded areas are indicators of the uncertainty and are derived through the bootstrapping technique with replacement introduced in the method section. Stars indicate months with significant change at the 5% level.

425 While the annual cycles for the two historical and RCP8.5 simulations are rela-
 426 tively similar to each other (Fig. 8), the representation of the diurnal cycle by these
 427 two sets of simulations largely differ (Fig. 9) with differences throughout the day
 428 except in the early morning with both parameterizations showing an increase in
 429 flash rate. The increasing occurrence of large-scale driven convection, which tends
 430 to occur homogeneously throughout the day in central Europe, or the occurrence of
 431 convective events that favors flash rate occurrence could explain this increase. The
 432 development of resampling techniques (e.g., resampling based on weather types),
 433 which are outside the scope of this study, may help test these hypotheses. During
 434 the afternoon, the two parameterizations disagree on the projection with a signif-
 435 icant decrease for the LPI and a significant increase for the $\text{CAPE} \times \text{PREC}$. This

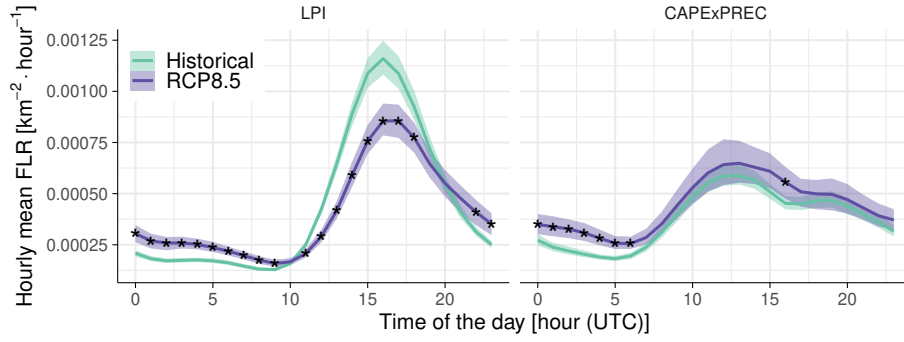


Fig. 9: Diurnal cycle of the hourly mean flash rate for the COSMO EC-Earth historical (green) and the EC-Earth future driven simulations (purple). The output of the LPI parameterization is shown on the left, while that of the CAPE \times PREC is shown on the right. The shaded areas indicate the uncertainty derived through the bootstrapping technique with replacement introduced in the method section. Stars indicate hours with a significant change at the 5% level.

436 disagreement is observed for most months featuring a mid-afternoon peak in flash
 437 rate (Fig. 10).

438 The increase of temperature between the historical and the RCP8.5 simulations
 439 is 3.3K (in both the CPS and the 0.22° simulations) for the full year and of
 440 similar amplitude for the convective season (here taken from April to September
 441 included - 3.3K). Assuming that the temperature scaling described in Section 3.1
 442 stays unchanged in the RCP8.5 scenario, the temperature increase found in the
 443 RCP8.5 scenario should result in increased flash rates. This assumption mostly
 444 holds for the CAPE \times PREC resulting in the total increase described in previous
 445 paragraphs. In contrast, the LPI scaling with temperature significantly differs in
 446 the RCP8.5 simulations (Fig. 11) compared to that in the historical simulation

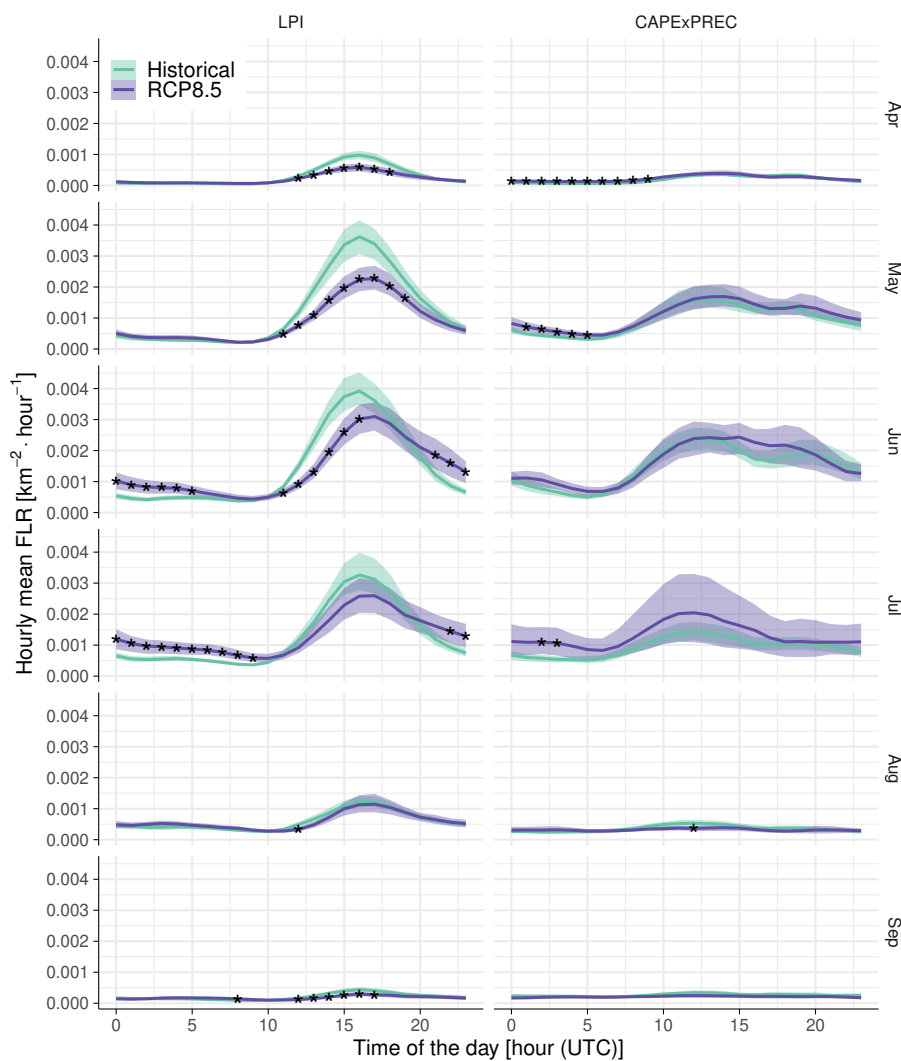


Fig. 10: Diurnal cycle of the hourly mean flash rate for the COSMO EC-Earth historical (green) and the EC-Earth future driven simulations (purple). The output of the LPI parameterization is shown on the left, while that of the CAPE \times PREC is shown on the right. Besides, each row shows the diurnal cycle for a given convectively active month (i.e., from April to September). The shaded areas indicate the uncertainty derived through the bootstrapping technique with replacement introduced in the method section. Stars indicate hours with a significant change at the 5% level.

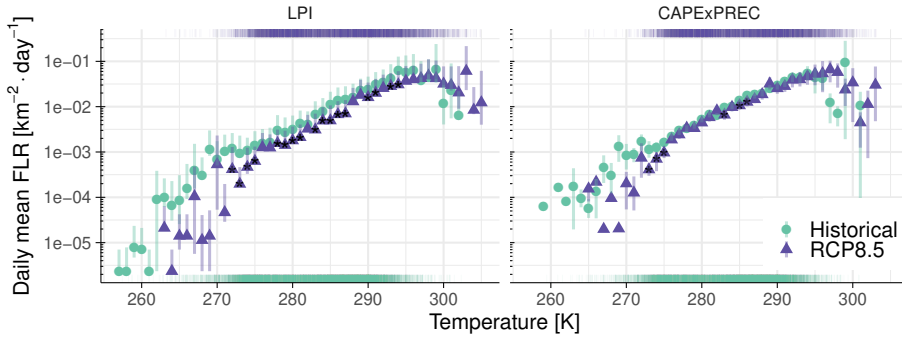


Fig. 11: The dependency of the mean daily flash rate with daily mean temperature for the COSMO EC-Earth historical driven simulation (green) and the EC-Earth future driven simulation (purple). The rugs at the bottom and the top of the plot show the occurrence of a given temperature for the corresponding simulation. Flash rates are binned to temperature values (i.e., one point per 1 K). These values are plotted for both the LPI (left column) and the CAPE \times PREC (right column) parameterizations. Stars indicate significant differences between the two simulations at the 5% level. This significance is only indicated for points for which the sample size exceeds 100 days.

447 with lower flash rates for a given temperature. Most of the significant changes
 448 occur for temperatures ranging from 278 K to 294 K. This decrease in the scaling
 449 occurs mainly in the afternoon, while the decrease is limited to a few bins in the
 450 morning (Fig. S2 in supplemental material).

451 4 Discussion

452 Section 3.2 describes the disagreement in the flash rate projection as represented
 453 by the LPI and the CAPE \times PREC parameterizations. The CAPE \times PREC

454 parameterization produces a spatiotemporally homogeneous increase in the flash
 455 rate that can be related to the temperature change. In contrast, the LPI shows
 456 unexpected results, with (i) a decrease of summer afternoon flash rates and (ii)
 457 a change of the projected flash rate temperature scaling compared to that of the
 458 historical simulation. In this section, the plausible causes for these unexpected
 459 results are investigated. For this, each input variable used in the LPI and the
 460 CAPE×PREC parameterizations was generated for three years (the years with
 461 the lowest, median and highest averaged LPI) in each EC-Earth driven simulation.
 462 While the comparison of these years is not long enough to reflect a climatology,
 463 it can still help to understand how the different input variables may influence the
 464 LPI. As a simple analysis of each input variable may lead to inconsistent results
 465 due to the non-linear properties of the LPI parameterization, the role of each input
 466 variable is investigated using the following formulas:

$$LPI_{base} = f_1 f_2 \frac{1}{H_{-20^\circ C} - H_{0^\circ C}} \int_{H_{0^\circ C}}^{H_{-20^\circ C}} g(w) dz \quad (10)$$

$$LPI_{no\epsilon} = f_1 f_2 \frac{1}{H_{-20^\circ C} - H_{0^\circ C}} \int_{H_{0^\circ C}}^{H_{-20^\circ C}} w^2 g(w) dz \quad (11)$$

$$LPI_{no w^2} = f_1 f_2 \frac{1}{H_{-20^\circ C} - H_{0^\circ C}} \int_{H_{0^\circ C}}^{H_{-20^\circ C}} \epsilon g(w) dz \quad (12)$$

469 All of these formulas are similar to that of the original parameterization except for
 470 the factors that are set to one. The LPI_{base} has the w and ϵ set equal to one and
 471 therefore mainly represent the effect of the different filters. $LPI_{no\epsilon}$ and $LPI_{no w^2}$
 472 have ϵ and w , respectively, set to one so that the effect of the vertical updraft or
 473 the microphysics can be investigated independently. Each formula is applied to

LPI	LPI_{base}	$LPI_{no\epsilon}$	LPI_{now^2}
-5.6%	-14.1%	-10.9%	-18.8%

Table 1: Projected change between the historical and the RCP8.5 three-year simulations for different formulas related to the LPI parameterization

474 the three-year simulations mentioned above. These results are then averaged both
 475 spatially and temporally.

476 Applying this method results in the following: The LPI_{base} decreases by 14.1%
 477 (Table 1) in the RCP8.5 simulation compared to that historical. The filters, which
 478 select the convective activity that favors lightning occurrence, therefore, tend to
 479 project a decrease of LPI. Adding the effect of the updraft results (i.e., using
 480 $LPI_{no\epsilon}$) in a reduced decrease of 10.9%. Finally, adding the effect of the micro-
 481 physics (i.e., using LPI_{now^2}) results in a further decrease of 18.8%. Based on these
 482 results, we hypothesize that both the filter and the microphysics factors of the LPI
 483 parameterization are responsible for the decrease in the projected LPI described in
 484 Section 3.2. In contrast, the updraft factor mitigates this decrease. In fact, for the
 485 three-year simulations, the full LPI parameterization results in a decrease of 5.6%,
 486 showing that for grid-points with high epsilon, the future simulation produces even
 487 higher updraft speed for the future simulation compared to that historical.

488 Similarly, the CAPE \times PREC parameterizations can be decomposed into dif-
 489 ferent factors. It notably shows a high degree of similarity with the $LPI_{no\epsilon}$; it
 490 incorporates a filter, through precipitation occurrence, and an indicator of the
 491 updraft intensity, through both precipitation intensity and $CAPE$. For the two
 492 selections of three years, the CAPE and precipitation variables were generated by
 493 both the 0.22° RCM and the CPM. The occurrence of precipitation's accumula-

Model Resolution	$CAPE \times PREC$	$CAPE$	$PREC$ occurrence
0.22°	31.3%	37.9%	4.0%
0.025° (CPM)	8.7%	7.8%	-3.8%

Table 2: Projected change between the historical and the RCP8.5 three-year simulations for different factors related to the $CAPE \times PREC$ parameterization

tion greater than 1.5 mm/hour, a threshold that results in an equivalent modeled
number of precipitation events as events with flashes for the evaluation period, is
decreasing by 3.8% (Table 2) in the CPM projection. For these events, the mean
CAPE increases by 7.8% in the CPM projection, resulting in a $CAPE \times PREC$
increase of 8.7%. In opposition to the CPM, in the 0.22° RCM projection, the
precipitation occurrence above 1.5 mm/hour shows an increase of 4.0%. Besides,
the CAPE, for the events above 1.5 mm/hour, shows a more substantial increase
in the 0.22° RCM projection compared to that in the CPM, with +37.9% change
resulting in a change of $CAPE \times PREC$ of +31.3%. This result suggests that the
CPM, as opposed to the 0.22° RCM, is partly responsible for the disagreement
observed in Section 3.2 between the LPI and the $CAPE \times PREC$. Therefore, our
results support the use of a CPM, as well as accounting for the microphysical
mixing for projecting flash rates. Accounting for the microphysical mixing makes
the LPI one of the most physically consistent flash rate parameterizations applied
on climate scale at the convection-permitting scale. Interestingly, it provides a
different climate change signal than the $CAPE \times PREC$ in this study. Generally,
the present study agrees with previous findings. Indeed, while the literature con-
sidering convective activity as a proxy for lightning suggested a global increase
in lightning activity under a warmer climate ranging from 5 to 10% increase per

513 degree of warming (Price and Rind, 1994; Price, 2009; Krause et al., 2014; Romps
514 et al., 2014; Rädler et al., 2019), the few studies using a scheme, which include
515 microphysics related parameters showed little increase or even a global decrease in
516 lightning activity (Jacobson and Streets, 2009; Finney et al., 2018, 2020). However,
517 the literature also highlights heterogeneous lightning changes around the globe.
518 For example, for the area under investigation in the present study, Krause et al.
519 (2014) find a small decrease in lightning despite considering convective activity as
520 a proxy for lightning. Besides, the use of a single simulation and, therefore, single
521 CPMs/GCMs significantly weakens the robustness of the projections computed
522 in this study. Large ensembles of simulations that encompass multiple CPM and
523 GCM combinations would be needed to validate the divergence of the two types of
524 lightning schemes (i.e., scheme with or without microphysical parameters) under
525 a warmer climate.

526 While the LPI may sound more advanced than a more simple parameteriza-
527 tion, and therefore, more trustworthy, it is still suffering from some weaknesses.
528 First, although being more physically consistent than other parameterizations,
529 the LPI is still not fully representing the cloud electrification. Thus, more com-
530 plex and more realistic parameterizations are needed. Second, the microphysics
531 parameterizations still suffer from fundamental limitations in climate models even
532 at convection-permitting scales. The use of different microphysics schemes, in ad-
533 dition to different lightning parameterizations, may be required to provide more
534 robust conclusions as well as realistic projection ensembles of flash rates for the
535 future.

536 **5 Conclusion**

537 Representing lightning in climate models is still a challenge. While many param-
538 eterizations exist, they strongly rely on the representation of convective cloud
539 properties. Since about a decade, CPMs are applicable to climate time scales.
540 These CPMs allow lightning parameterizations closer to process understanding
541 than coarser-grid climate models that rely on a deep convection parameterization.
542 In this study, such a lightning parameterization, namely the LPI, was implemented
543 in the regional climate model COSMO-CLM. This model configuration was applied
544 to perform three simulations on a convection-permitting scale. The first simula-
545 tion uses ERA-Interim as driving data to adjust the LPI to observed flash rates
546 and an evaluation at different spatiotemporal scales. The additional two additional
547 simulations use EC-Earth global climate simulations as driving data allowing for
548 the investigation of the LPI evolution under the RCP8.5 scenario. The output
549 of the LPI parameterization for these simulations was compared to another flash
550 rate parametrization, namely the $\text{CAPE} \times \text{PREC}$, that was derived for non-CPM
551 corresponding simulations.

552 Our results show that the LPI parameterizations reproduce the present-day
553 daily and hourly probability densities, the latitudinal dependency, and the diurnal
554 cycle of the observed flash rates. While the $\text{CAPE} \times \text{PREC}$ parameterization pro-
555 duces correct representations of the temporal probability densities and the latitu-
556 dinal dependency, these representations are not as skillful as those derived with the
557 LPI. Furthermore, the diurnal cycle is poorly represented by the $\text{CAPE} \times \text{PREC}$
558 parameterization. Both parameterizations underestimate spatial heterogeneity. Fi-

559 nally, most of the observed temperature-scaling is realistically reproduced for both
560 parameterizations, confirming their applicability to climate projections.

561 A comparison of the EC-Earth driven simulations (historical 1975-2005 versus
562 RCP8.5 2071-2100) indicates a climate change signal in mean flash rate by -4.8%
563 as projected by the LPI and by $+17.4\%$ as projected by the CAPE \times PREC.
564 Both parameterizations generate more frequent extremely high flash rates (99.9th
565 percentile), but this increase is more substantial for the CAPE \times PREC. Both his-
566 torical and future simulations show similar annual cycles with higher flash rates in
567 summer than in winter. However, the LPI projects a decrease in flash rates while
568 the CAPE \times PREC shows a change of opposite sign. This decrease is related to
569 a decrease in flash rates produced during mid-afternoon convection. Finally, the
570 increase of flash rate found for the CAPE \times PREC can be related to the temper-
571 ature increase as the CAPE \times PREC temperature-scaling of flash rates remains
572 identical for both simulations. For the LPI, the temperature scaling is altered in
573 the RCP8.5 simulation showing possible limitations of temperature based rescaling
574 techniques for downscaling flash rates.

575 The investigation of potential sources of flash rate reduction revealed that both
576 the use of a CPM and accounting for microphysical mixing changes are likely causes
577 for the projected disagreements between the two flash rates parameterizations.
578 Changes in the updraft velocity partly compensate for the changes induced by the
579 microphysical mixing. These findings fit with the projected change in flash rate as
580 simulated by the CAPE \times PREC for which the increase in the vertical velocity is
581 carried through the increase in CAPE and precipitation accumulation, but does
582 not have any factors that can carry the signal of the microphysics mixing. Besides,
583 applying the CAPE \times PREC at the convection-permitting scale does not result in a

584 convergence of the projected flash rate with the LPI. This absence of convergence
585 points at the influence of the CPM on the differences observed between the two
586 flash rates parameterizations. Quantifying this influence is an important question
587 that still has to be answered. The use of a broader range of parameterizations
588 applied in both multiple CPM and non-CPM model may help to provide elements
589 of answers to this question.

590 Besides, applying the CAPE \times PREC at the convection-permitting scale does
591 not result in a convergence of the projected flash rate with the LPI. This absence of
592 convergence points at the influence of the CPM on the differences observed between
593 the two flash rate parameterizations. Quantifying this influence is an important
594 question that still has to be answered. The use of a broader range of parameteriza-
595 tions applied in both multiple CPMs and non-CPMs may help to provide elements
596 of answers to this question. Furthermore, using a single CPM/RCM driven, by only
597 one global climate model and one reanalysis, of one parameterization, and for a
598 specific region does not allow for deriving robust lightning climate projections.
599 Still, this study shows that explicitly accounting for the microphysics in flash rate
600 parameterizations as well as representing explicitly and more robustly convective
601 processes using convection-permitting models potentially improve current climate
602 projections of lightning.

603 **Acknowledgements** This research has been partially funded by TLUG, Thüringen, by LAU,
604 Sachsen-Anhalt, by HLNUG, Hessen, by FAWF, Rheinland-Pfalz, by the French National Re-
605 search Agency under the future investment program ANR-18-MPGA-0005, and by the EUCP
606 project which is funded by the European Commission through the Horizon 2020 Programme
607 for Research and Innovation (Grant Agreement 776613). The computational resources have
608 been provided by the LOEWE-CSC.

609 **Data availability** The data and materials used in this study are available upon
 610 request to the corresponding author except from the observed dataset and the
 611 COSMO-CLM model source code. The latter can be obtained by becoming a
 612 member of the CLM community.

613 **A Filtering of noisy weak LPI signals (f_1)**

614 As already noted in Yair et al. (2010), weak and noisy LPI signals caused by isolated single-
 615 grid-column updrafts may occur in km-scale models, which do not fully resolve small-scale
 616 convective updrafts. Because such situations do not really represent physically coherent con-
 617 vective updrafts, valid positive LPI values are restricted to grid-points for which the majority
 618 of grid columns in a certain horizontal neighborhood exhibits a maximum updraft speed above
 619 a certain threshold (Yair et al., 2010). This criterion is adapted in the boolean filter function
 620 f_1 in Eq. (1)

$$f_1 = \begin{cases} 1 & \text{if } a \geq 0.5 \\ 0 & \text{else} \end{cases} \quad (13)$$

621 with the area fraction a in a $10 \times 10 \text{ km}^2$ neighbourhood with column maximum updrafts
 622 larger than a threshold $w_{(max,0)}$,

$$a = \frac{\iint_{S=10 \times 10 \text{ km}^2} \begin{cases} 1 & \text{if } \max(w(z)) \geq w_{(max,0)} \\ 0 & \text{else} \end{cases} dx dy}{\iint_{S=10 \times 10 \text{ km}^2} dx dy} . \quad (14)$$

623 $w_{(max,0)}$ is set to 1.1 m/s in our application, a value which was found to produce reasonable
 624 spatial LPI distributions in comparison to observed flash rates.

625 **B Filtering of false LPI signals in strong orographic gravity wave clouds**

626 (f_2)

627 The filter f_1 is not enough to prevent spurious LPI signals in deep orographic wave clouds,
 628 which have been noted during the implementation work, for example, during Föhn events in

629 the Alps in winter time. Large-amplitude gravity waves embedded in moist flow may lead to
 630 small but spurious graupel formation in cloud microphysics schemes, which in turn leads to
 631 false LPI signals. To prevent this, a second boolean function f_2 has been added, which is based
 632 on the fact that gravity waves require a rather stable stratification throughout the troposphere.
 633 f_2 is defined as the column-integrated buoyancy in a $20 \times 20 \text{ km}^2$ neighbourhood:

$$f_2 = \left\{ \begin{array}{ll} 1 & \text{if } B_{ML} \geq B_0 \\ 0 & \text{else} \end{array} \right\} \quad (15)$$

634 with

$$B_{ML} = \frac{\iint_{S=20 \times 20 \text{ km}^2} \int_{p_s-550 \text{ hPa}}^{p_s-50 \text{ hPa}} R_d (T_{v,parcel} - T_{v,s}) d \ln p dx dy}{\iint_{S=20 \times 20 \text{ km}^2} dx dy} \quad (16)$$

635 where p is the pressure, p_s the surface pressure, R_d the gas constant of dry air, $T_{v,parcel}$
 636 the virtual temperature of a moist adiabatic parcel ascent starting from 50 hPa above ground
 637 with average properties of the lowermost 100 hPa and $T_{v,s}$ local virtual temperature. B_{ML}
 638 is formally similar to mixed layer CAPE, but with fixed integration over a 500 hPa layer
 639 starting at 50 hPa above ground. B_{ML} is approximately 0 or slightly negative at locations of
 640 explicitly simulated convective cells, but attains large negative values for the stable conditions
 641 associated with orographic mountain waves. The threshold value and $B_0 = -1500 \text{ J/kg}^2$ was
 642 found by experimentation to reasonably separate these two regimes for our CPM domain over
 643 Central Europe.

644 References

- 645 Baldauf, M., A. Seifert, J. Förstner, D. Majewski, M. Raschendorfer, and T. Rein-
 646 hardt (2011, dec). Operational Convective-Scale Numerical Weather Prediction
 647 with the COSMO Model: Description and Sensitivities. *Monthly Weather Re-*
 648 *view* 139(12), 3887–3905.
- 649 Ban, N., J. Schmidli, and C. Schaer (2014, jul). Evaluation of the convection-
 650 resolving regional climate modelling approach in decade-long simulations. *Jour-*
 651 *nal of Geophysical Research: Atmospheres* 119(13), 7889–7907.

- 652 Barthe, C., M. Chong, J. P. Pinty, C. Bovalo, and J. Escobar (2012). CELLS v1.0:
653 Updated and parallelized version of an electrical scheme to simulate multiple
654 electrified clouds and flashes over large domains. *Geoscientific Model Develop-*
655 *ment* 5(1), 167–184.
- 656 Barthe, C. and J. P. Pinty (2007). Simulation of a supercellular storm using
657 a three-dimensional mesoscale model with an explicit lightning flash scheme.
658 *Journal of Geophysical Research Atmospheres* 112(6), 1–12.
- 659 Blitz Information Dienst Siemens (2019). <https://new.siemens.com/global/de/produkte/services/blids.html>
660 accessed on 2020-01-31.
- 661 Böhm, U., M. Kücken, W. Ahrens, A. Block, D. Hauffe, K. Keuler, B. Rockel,
662 and A. Will (2006). CLM - The Climate Version of LM : Brief Description and
663 Long-Term Applications. Technical Report 6.
- 664 Brisson, E., C. Brendel, S. Herzog, and B. Ahrens (2018, jan). Lagrangian eval-
665 uation of convective shower characteristics in a convection-permitting model.
666 *Meteorologische Zeitschrift* 27(1), 59–66.
- 667 Brisson, E., M. Demuzere, and N. P. Van Lipzig (2016). Modelling strate-
668 gies for performing convection-permitting climate simulations. *Meteorologische*
669 *Zeitschrift* 25(2), 149–163.
- 670 Brisson, E., K. Van Weverberg, M. Demuzere, A. Devis, S. Saeed, M. Stengel, and
671 N. P. van Lipzig (2016). How well can a convection-permitting climate model
672 reproduce decadal statistics of precipitation, temperature and cloud character-
673 istics? *Climate Dynamics* 47(9-10), 3043–3061.
- 674 Chepfer, H., V. Noel, D. Winker, and M. Chiriaco (2014). Where and when
675 will we observe cloud changes due to climate warming?. *Geophysical Research*
676 *Letters* 41(23), 8387–8395.

- 677 Clark, S. K., D. S. Ward, and N. M. Mahowald (2017, mar). Parameterization-
678 based uncertainty in future lightning flash density. *Geophysical Research Let-*
679 *ters* 44(6), 2893–2901.
- 680 Doms, G., J. Forstner, E. Heis, H. J. Herzog, M. Raschendorfer, T. Reinhardt,
681 B. Ritter, R. Schrodin, J. P. Schulz, and G. Vogel (2011). A Description of the
682 Nonhydrostatic Regional COSMO Model Part II : Physical Parameterization.
683 Technical Report September.
- 684 Fierro, A. O., E. R. Mansell, D. R. Macgorman, and C. L. Ziegler (2013). The
685 implementation of an explicit charging and discharge lightning scheme within
686 the wrf-arw model: Benchmark simulations of a continental squall line, a tropical
687 cyclone, and a winter storm. *Monthly Weather Review* 141(7), 2390–2415.
- 688 Finney, D. L., R. M. Doherty, O. Wild, and N. L. Abraham (2016). The im-
689 pact of lightning on tropospheric ozone chemistry using a new global lightning
690 parametrisation. *Atmospheric Chemistry and Physics* 16(12), 7507–7522.
- 691 Finney, D. L., R. M. Doherty, O. Wild, H. Huntrieser, H. C. Pumphrey, and
692 A. M. Blyth (2014). Using cloud ice flux to parametrise large-scale lightning.
693 *Atmospheric Chemistry and Physics* 14(23), 12665–12682.
- 694 Finney, D. L., R. M. Doherty, O. Wild, D. S. Stevenson, I. A. MacKenzie, and
695 A. M. Blyth (2018). A projected decrease in lightning under climate change.
696 *Nature Climate Change* 8(3), 210–213.
- 697 Finney, D. L., J. H. Marsham, J. M. Wilkinson, P. R. Field, A. M. Blyth, L. S. Jack-
698 son, E. J. Kendon, S. O. Tucker, and R. A. Stratton (2020). African Lightning
699 and its Relation to Rainfall and Climate Change in a Convection-Permitting
700 Model. *Geophysical Research Letters* 47(23).

- 701 Helsen, S., N. P. van Lipzig, M. Demuzere, S. Vanden Broucke, S. Caluwaerts,
702 L. De Cruz, R. De Troch, R. Hamdi, P. Termonia, B. Van Schaeybroeck, and
703 H. Wouters (2020). Consistent scale-dependency of future increases in hourly
704 extreme precipitation in two convection-permitting climate models. *Climate*
705 *Dynamics* 54(3-4), 1267–1280.
- 706 Houze, R. A. (1993). *Cloud Dynamics*. International Geophysics Series.
- 707 Houze, R. A. (2014). *Cloud Dynamics* (2nd Editio ed.). Academic Press.
- 708 Jacobson, M. Z. and D. G. Streets (2009). Influence of future anthropogenic
709 emissions on climate, natural emissions, and air quality. *Journal of Geophysical*
710 *Research Atmospheres* 114(8), 1–21.
- 711 Jayaratne, E. R., C. P. Saunders, and J. Hallett (1983). Laboratory studies of
712 the charging of soft-hail during ice crystal interactions. *Quarterly Journal of the*
713 *Royal Meteorological Society* 109(461), 609–630.
- 714 Keller, M., O. Fuhrer, J. Schmidli, M. Stengel, R. Stöckli, and C. Schär (2016).
715 Evaluation of convection-resolving models using satellite data: The diurnal cycle
716 of summer convection over the Alps. *Meteorologische Zeitschrift* 25(2), 165–179.
- 717 Kendon, E. J., N. Ban, N. M. Roberts, H. J. Fowler, M. J. Roberts, S. C. Chan,
718 J. P. Evans, G. Fossier, and J. M. Wilkinson (2016). Do Convection-Permitting
719 Regional Climate Models Improve Projections of Future Precipitation Change?
720 *Bulletin of the American Meteorological Society* 98(1), 79–93.
- 721 Kendon, E. J., N. M. Roberts, H. J. Fowler, M. J. Roberts, S. C. Chan, and C. a.
722 Senior (2014, jun). Heavier summer downpours with climate change revealed
723 by weather forecast resolution model. *Nature Climate Change* 4(7), 570–576.
- 724 Krause, A., S. Kloster, S. Wilkenskjeld, and H. Paeth (2014). The sensitivity
725 of global wildfires to simulated past, present, and future lightning frequency.

- 726 *Journal of Geophysical Research: Biogeosciences* 119(3), 312–322.
- 727 Lagasio, M., A. Parodi, R. Procopio, F. Rachidi, and E. Fiori (2017). Lightning
728 potential index performances in multimicrophysical cloud-resolving simulations
729 of a back-building mesoscale convective system: The Genoa 2014 event. *Journal*
730 *of Geophysical Research* 122(8), 4238–4257.
- 731 Latham, J., W. A. Petersen, W. Deierling, and H. J. Christian (2007). Field iden-
732 tification of a unique globally dominant mechanism of thunderstorm electrifica-
733 tion. *Quarterly Journal of the Royal Meteorological Society* 133(627), 1453–1457.
- 734 Leutwyler, D., D. Lüthi, N. Ban, O. Fuhrer, and C. Schär (2017). Evaluation of the
735 convection-resolving climate modeling approach on continental scales. *Journal*
736 *of Geophysical Research* 122(10), 5237–5258.
- 737 Lopez, P. (2016). A lightning parameterization for the ECMWF Integrated Fore-
738 casting System. *Mon. Wea. Rev.* 144(9), 3057–3075.
- 739 Lynn, B. and Y. Yair (2010, feb). Prediction of lightning flash density with the
740 WRF model. *Advances in Geosciences* 23, 11–16.
- 741 McCaul, E. W., S. J. Goodman, K. M. LaCasse, and D. J. Cecil (2009). Fore-
742 casting lightning threat using cloud-resolving model simulations. *Weather and*
743 *Forecasting* 24(3), 709–729.
- 744 Murphy, A. H. (1988). Skill Scores Based on the Mean Square Error and Their
745 Relationships to the Correlation Coefficient. *Monthly Weather Review* 116(12),
746 2417–2424.
- 747 Perkins, S. E., a. J. Pitman, N. J. Holbrook, and J. McAneney (2007). Evaluation
748 of the AR4 Climate Models’ Simulated Daily Maximum Temperature, Mini-
749 mum Temperature, and Precipitation over Australia Using Probability Density
750 Functions. *Journal of Climate* 20(17), 4356–4376.

- 751 Prein, A. F., G. J. Holland, R. M. Rasmussen, J. Done, K. Ikeda, M. P. Clark,
752 and C. H. Liu (2013). Importance of Regional Climate Model Grid Spacing for
753 the Simulation of Heavy Precipitation in the Colorado Headwaters. *Journal of*
754 *Climate* 26(13), 4848–4857.
- 755 Prein, A. F., W. Langhans, G. Fosser, A. Ferrone, N. Ban, K. Goergen, M. Keller,
756 M. Tölle, O. Gutjahr, F. Feser, E. Brisson, S. Kollet, J. Schmidli, N. P. M. van
757 Lipzig, and R. Leung (2015, jun). A review on regional convection-permitting
758 climate modeling: Demonstrations, prospects, and challenges. *Reviews of Geo-*
759 *physics* 53(2), 323–361.
- 760 Price, C. (2009). Will a drier climate result in more lightning? *Atmospheric Re-*
761 *search* 91(2-4), 479–484.
- 762 Price, C. and D. Rind (1992). A simple lightning parameterization for calcu-
763 lating global lightning distributions. *Journal of Geophysical Research: Atmo-*
764 *spheres* 97(D9), 9919–9933.
- 765 Price, C. and D. Rind (1994). Possible implications of global climate change
766 on global lightning distributions and frequencies. *Journal of Geophysical Re-*
767 *search* 99(D5).
- 768 Rädler, A. T., P. H. Groenemeijer, E. Faust, R. Sausen, and T. Púčik (2019).
769 Frequency of severe thunderstorms across Europe expected to increase in the
770 21st century due to rising instability. *npj Climate and Atmospheric Science* 2(1),
771 3–7.
- 772 Reynolds, S. E., M. Brook, and M. F. Gourley (1957, oct). THUNDERSTORM
773 CHARGE SEPARATION. *Journal of Meteorology* 14(5), 426–436.
- 774 Rockel, B., A. Will, and A. Hense (2008). The Regional Climate Model COSMO-
775 CLM (CCLM). *Meteorologische Zeitschrift* 17(4), 347–348.

- 776 Romps, D. M., J. T. Seeley, D. Vollaro, and J. Molinari (2014). Projected increase
777 in lightning strikes in the United States due to global warming. *Science* 346(621),
778 851–853.
- 779 Saunders, C. (2008). Charge separation mechanisms in clouds. *Space Science*
780 *Reviews* 137(1-4), 335–353.
- 781 Saunders, C. P. and S. L. Peck (1998). Laboratory studies of the influence of the
782 rime accretion rate on charge transfer during crystal/graupel collisions. *Journal*
783 *of Geophysical Research Atmospheres* 103(D12), 13949–13956.
- 784 Saunders, C. P. R. (1993, apr). A Review of Thunderstorm Electrification Pro-
785 cesses. *Journal of Applied Meteorology* 32(4), 642–655.
- 786 Schulz, W. and G. Diendorfer (2004). Performance Improvement of the German
787 Lightning Location System during the 11 Years of Operation. In *27th Inter-*
788 *national Conference on Lightning Protection (27th ICLP)*, Avignon, France, pp.
789 1–4.
- 790 Sokol, Z. and J. Minarova (2020). Impact of 1- and 2-moment cloud microphysics
791 and horizontal resolution on Lightning Potential Index within COSMO NWP
792 model. *Atmos. Res.* 237, 104862.
- 793 Steppeler, J., G. Doms, U. Schaettler, H. W. Bitzer, A. Gassmann, U. Damrath,
794 G. Gregoric, U. Schättler, H. W. Bitzer, A. Gassmann, U. Damrath, and G. Gre-
795 goric (2003, jan). Meso-gamma scale forecasts using the nonhydrostatic model
796 LM. *Meteorology and Atmospheric Physics* 82(1-4), 75–96.
- 797 Stolzenburg, M., W. D. Rust, and T. C. Marshall (1998a). Electrical structure
798 in thunderstorm convective regions 2. Isolated storms. *Journal of Geophysical*
799 *Research Atmospheres* 103(D12), 14079–14096.

- 800 Stolzenburg, M., W. D. Rust, and T. C. Marshall (1998b). Electrical structure
801 in thunderstorm convective regions 2. Isolated storms. *Journal of Geophysical*
802 *Research Atmospheres* 103(D12), 14079–14096.
- 803 Stolzenburg, M., W. D. Rust, and T. C. Marshall (1998c). Electrical structure in
804 thunderstorm convective regions 3. Synthesis. *Journal of Geophysical Research*
805 *Atmospheres* 103(D12), 14097–14108.
- 806 Takahashi, T. (1978, aug). Riming Electrification as a Charge Generation Mech-
807 anism in Thunderstorms. *Journal of the Atmospheric Sciences* 35(8), 1536–1548.
- 808 Tiedtke, M. (1989). A comprehensive mass flux scheme for cumulus parameteri-
809 zation in large-scale models. *Mon. Wea. Rev.* 117, 1779–1799.
- 810 Vanden Broucke, S., H. Wouters, M. Demuzere, and N. P. M. van Lipzig (2019,
811 may). The influence of convection-permitting regional climate modeling on
812 future projections of extreme precipitation: dependency on topography and
813 timescale. *Climate Dynamics* 52(9-10), 5303–5324.
- 814 Williams, E. R. (1988, mar). The Electrification of Thunderstorms. *Scientific*
815 *American* 259(5), 88–99.
- 816 Yair, Y. (2008). Charge generation and separation processes. *Space Science Re-*
817 *views* 137(1-4), 119–131.
- 818 Yair, Y., B. Lynn, C. Price, V. Kotroni, K. Lagouvardos, E. Morin, A. Mugnai,
819 and M. Del Carmen Llasat (2010). Predicting the potential for lightning ac-
820 tivity in Mediterranean storms based on the Weather Research and Forecasting
821 (WRF) model dynamic and microphysical fields. *Journal of Geophysical Research*
822 *Atmospheres* 115(4), 1–13.
- 823 Yoshida, S., T. Morimoto, T. Ushio, and Z. I. Kawasaki (2009). A fifth-power rela-
824 tionship for lightning activity from Tropical Rainfall Measuring Mission satellite

825 observations. *Journal of Geophysical Research Atmospheres* 114(9), 1–10.

Figures

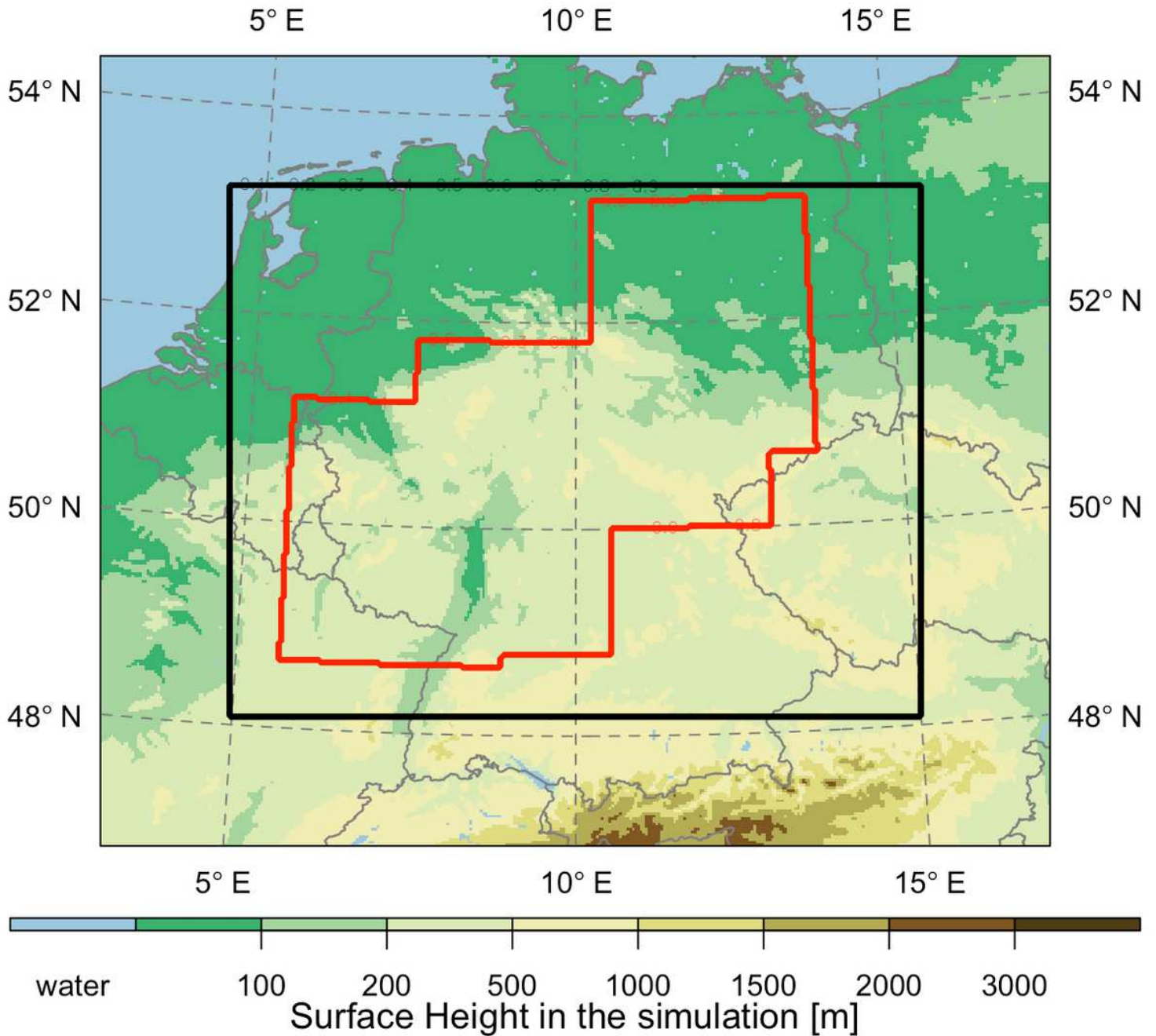


Figure 1

Domain of the 0:025° simulation. The red polygon indicates the area where observations are available and, therefore, also the evaluation domain. The black rectangle shows the domain used for the analyses other than the evaluation. Note: The designations employed and the presentation of the material on this map do not imply the expression of any opinion whatsoever on the part of Research Square concerning the legal status of any country, territory, city or area or of its authorities, or concerning the delimitation of its frontiers or boundaries. This map has been provided by the authors.

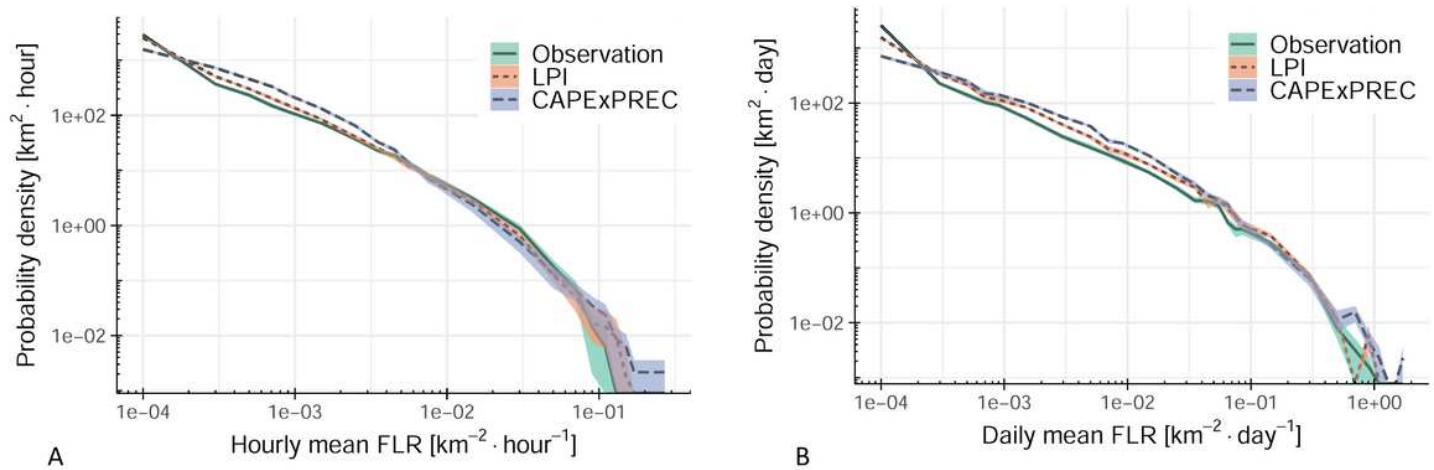


Figure 2

Probability densities of the domain average (a) hourly and (b) daily ash rates as observed (solid line), as represented by the LPI (short-dashed line), and by the CAPE × PREC (long-dashed line) parameterizations. The shaded areas represent the uncertainty derived through the bootstrapping technique with replacement introduced in the method section.

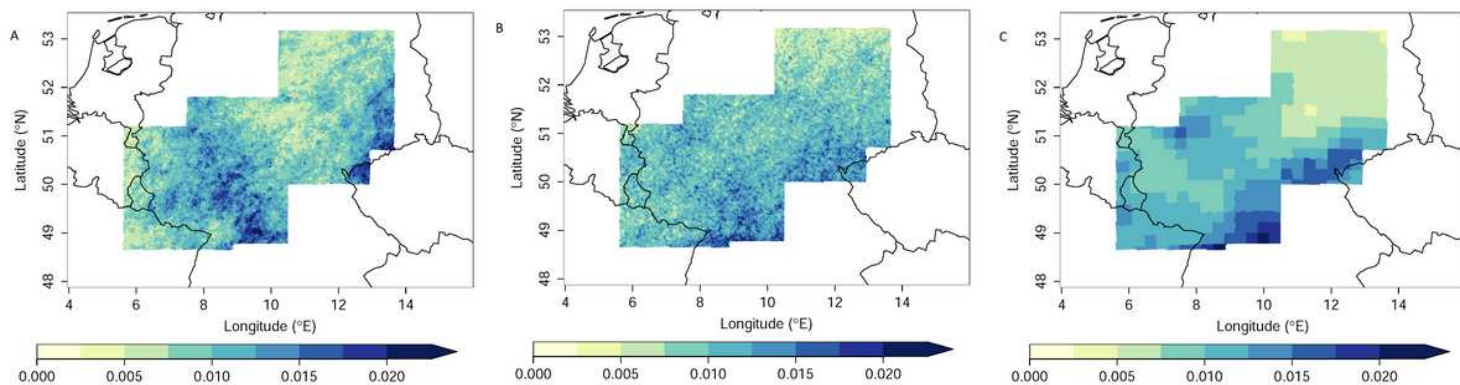


Figure 3

Spatial distribution of daily averaged observed and modeled ash rate (Flash $m^{-2} \text{ hour}^{-1}$) over the period 2000-2013.

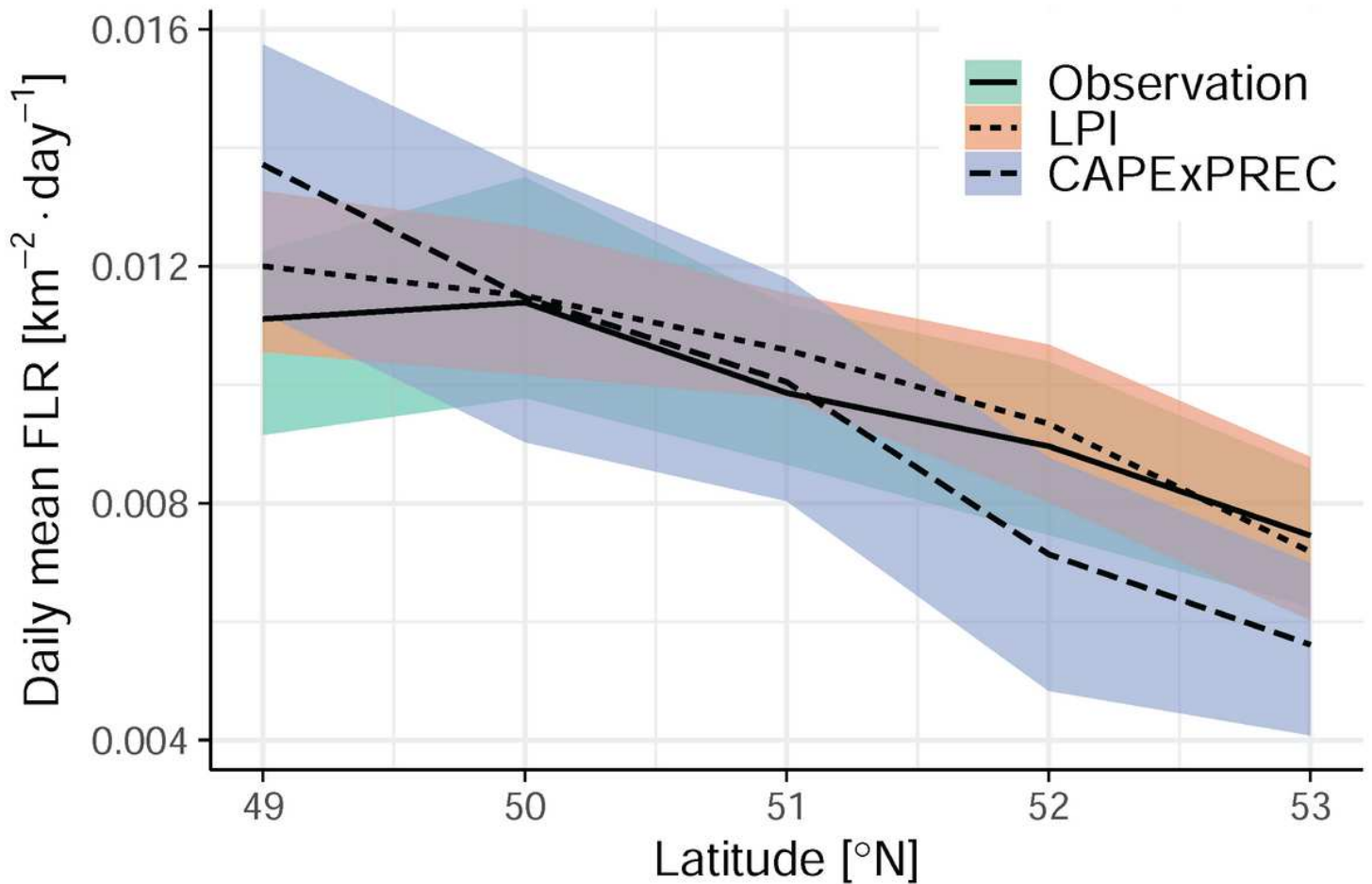


Figure 4

Latitudinal dependence of the daily ash rates for the period 2000-2013. The solid line indicates the observation while the dashed lines show the parameterizations output (short dash for the LPI and long dash for the CAPE \times PREC). The shaded areas provide the sampling uncertainty derived from 100 bootstraps with replacement.

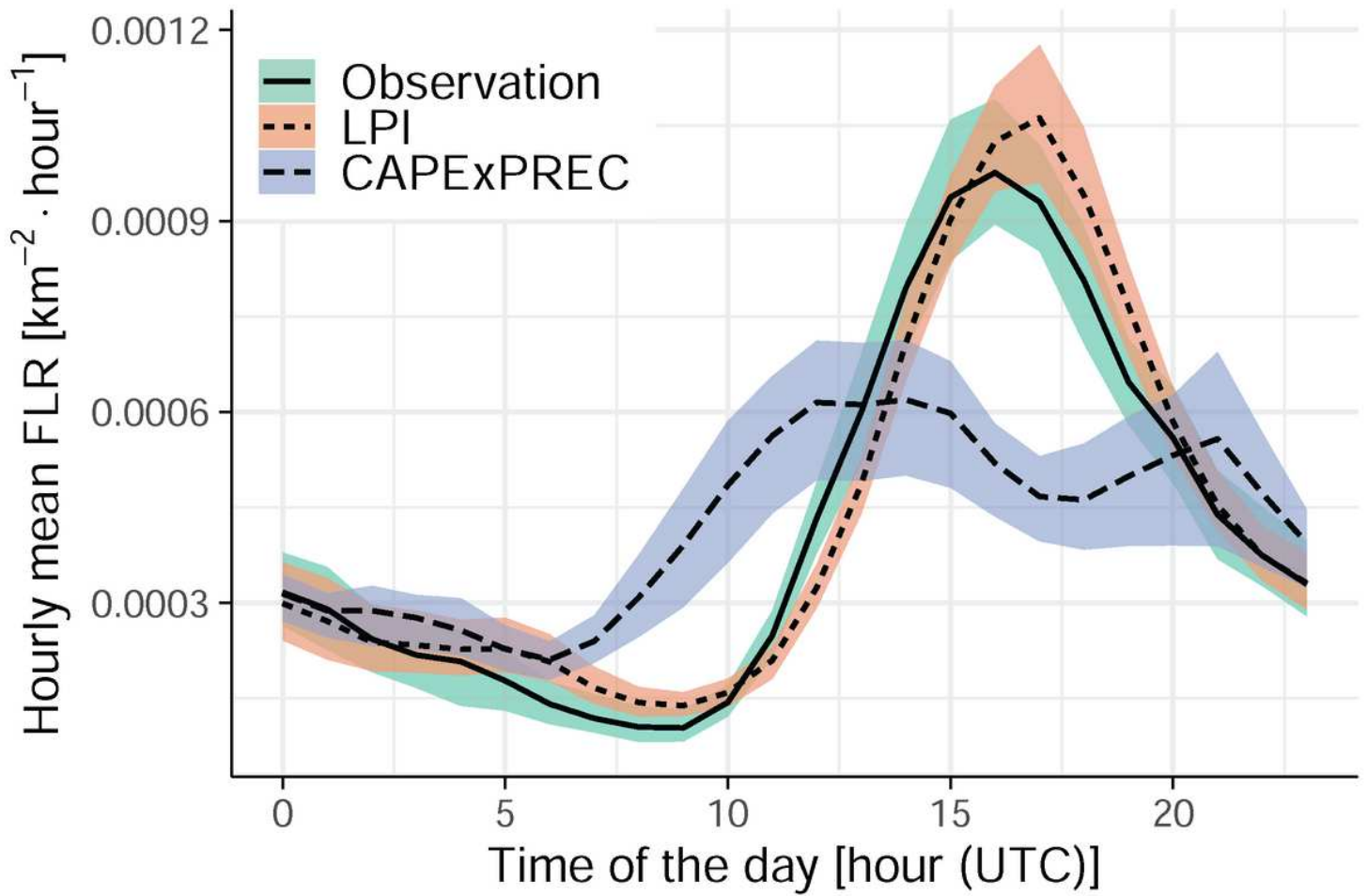


Figure 5

Diurnal cycle of the hourly ash rate averaged over the evaluation domain and the period 2000-2013. The solid line indicates the observation, while the shortdashed line shows the LPI, and the long-dashed line shows the CAPE×PREC diurnal cycles. The shaded areas provide the sampling uncertainty derived from 100 bootstraps with replacement.

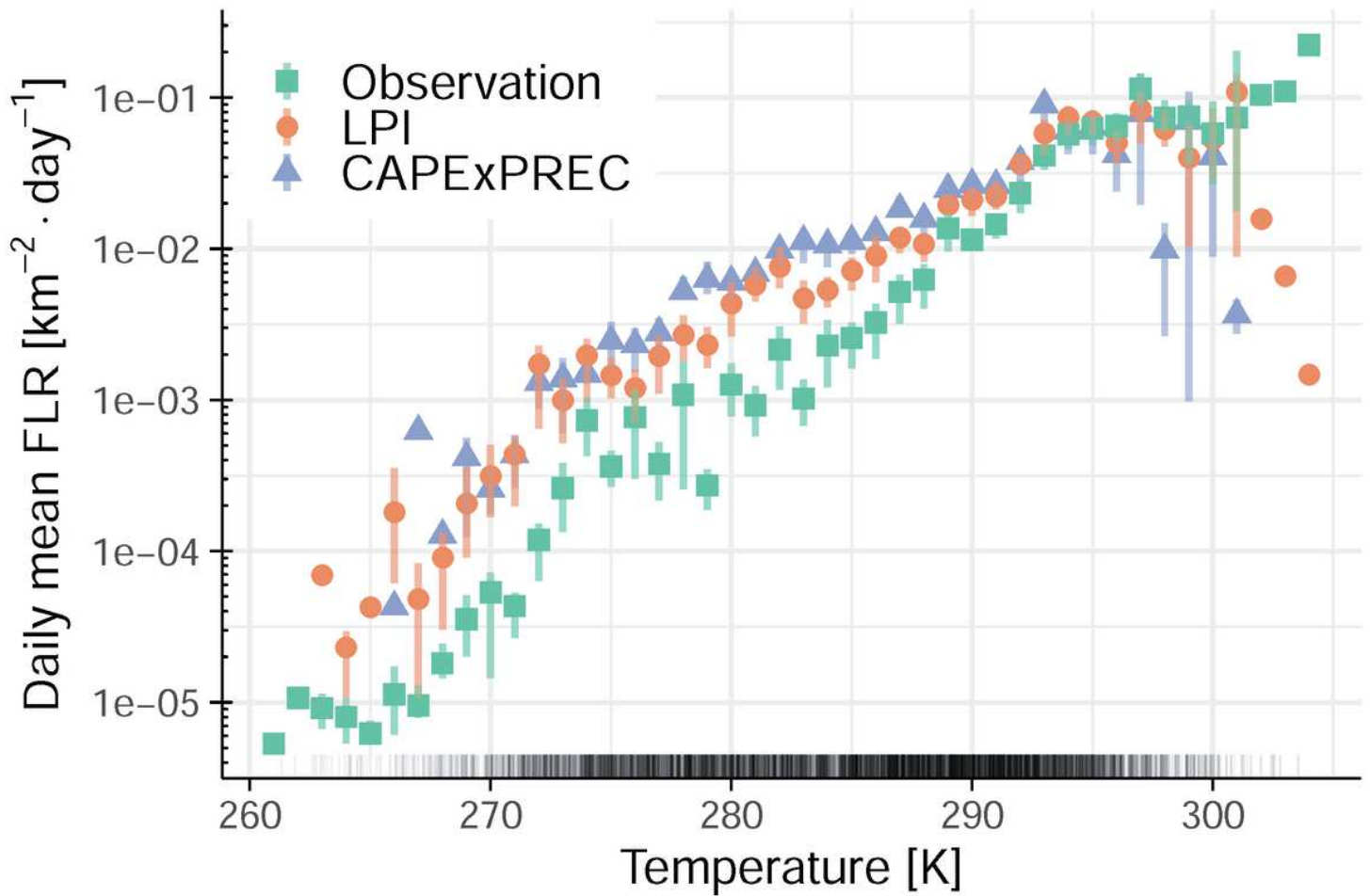


Figure 6

The dependency of domain-averaged daily mean ash rates with daily temperature for the period 2000-2013. The observation (green squares) and the parameterizations (orange circle for the LPI and blue triangle for the CAPE \times PREC) are binned to temperature classes (i.e., one value per 1K class). In addition, the corresponding bars provide the sampling uncertainty derived from 100 bootstraps with replacement when the sample size is larger than one. The rug at the bottom of the plot shows the simulated temperature values for the investigated period.

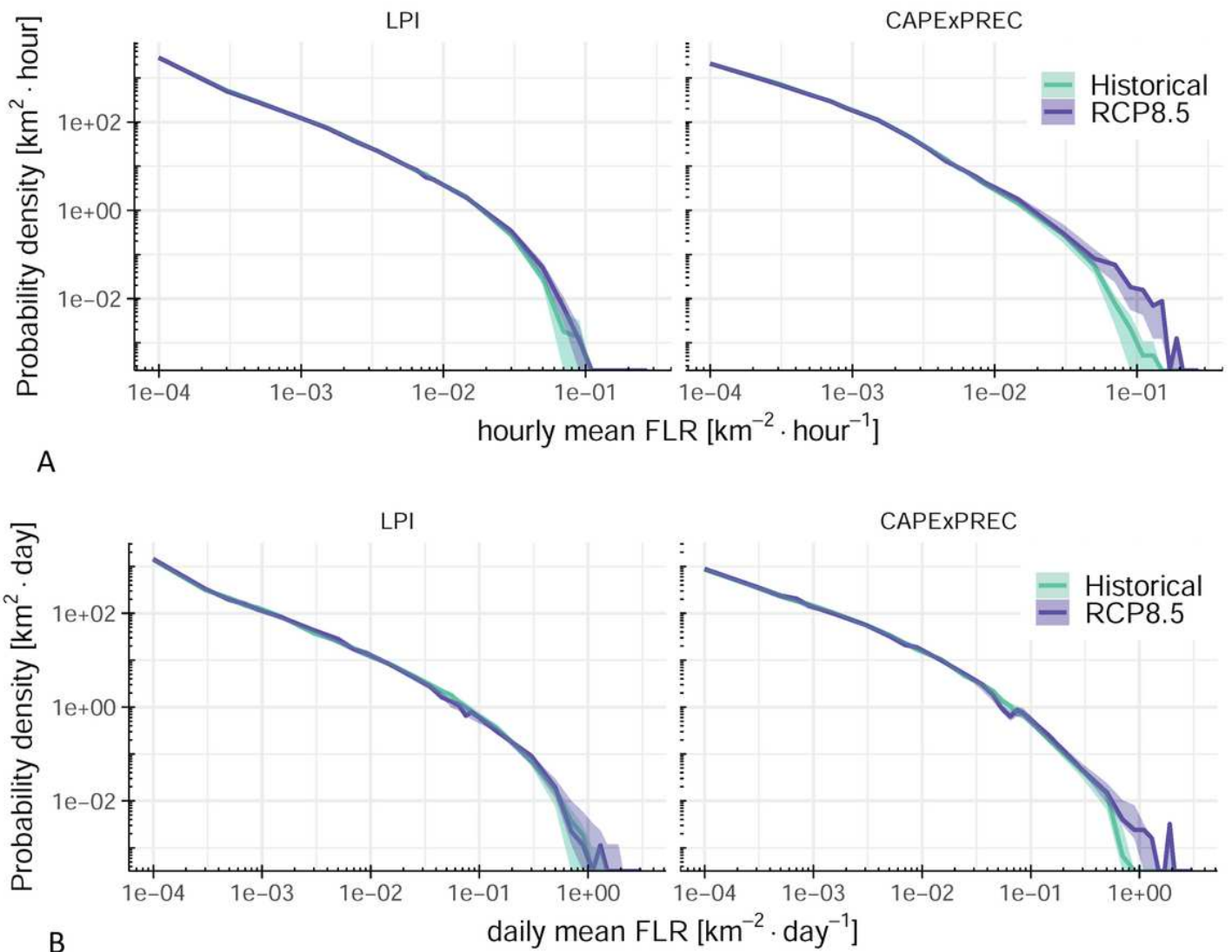


Figure 7

Probability densities of the domain average hourly ash rates (a) and domain average daily ash rates (b) as represented by the LPI and the CAPExPREC parameterizations for EC-Earth driven simulations. The shaded areas represent the uncertainty and are derived through the bootstrapping technique with replacement introduced in the method section.

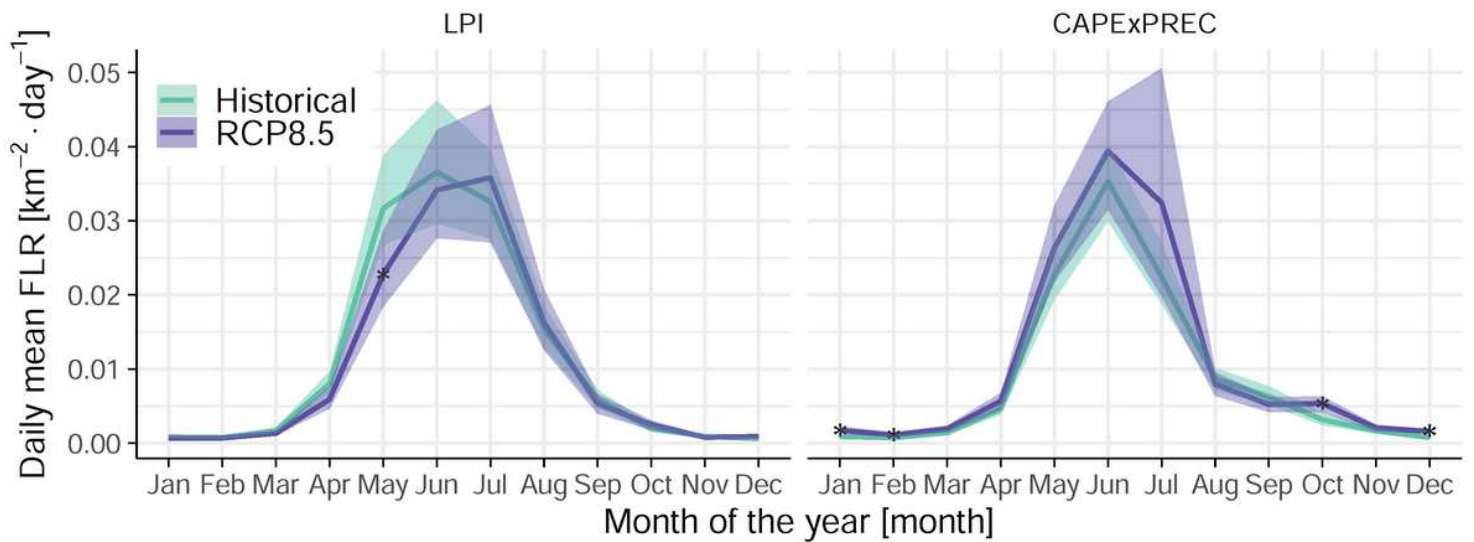


Figure 8

Annual cycle of the daily mean ash rate for the COSMO EC-Earth historical (green) and the EC-Earth future driven simulations (purple). The shaded areas are indicators of the uncertainty and are derived through the bootstrapping technique with replacement introduced in the method section. Stars indicate months with significant change at the 5% level.

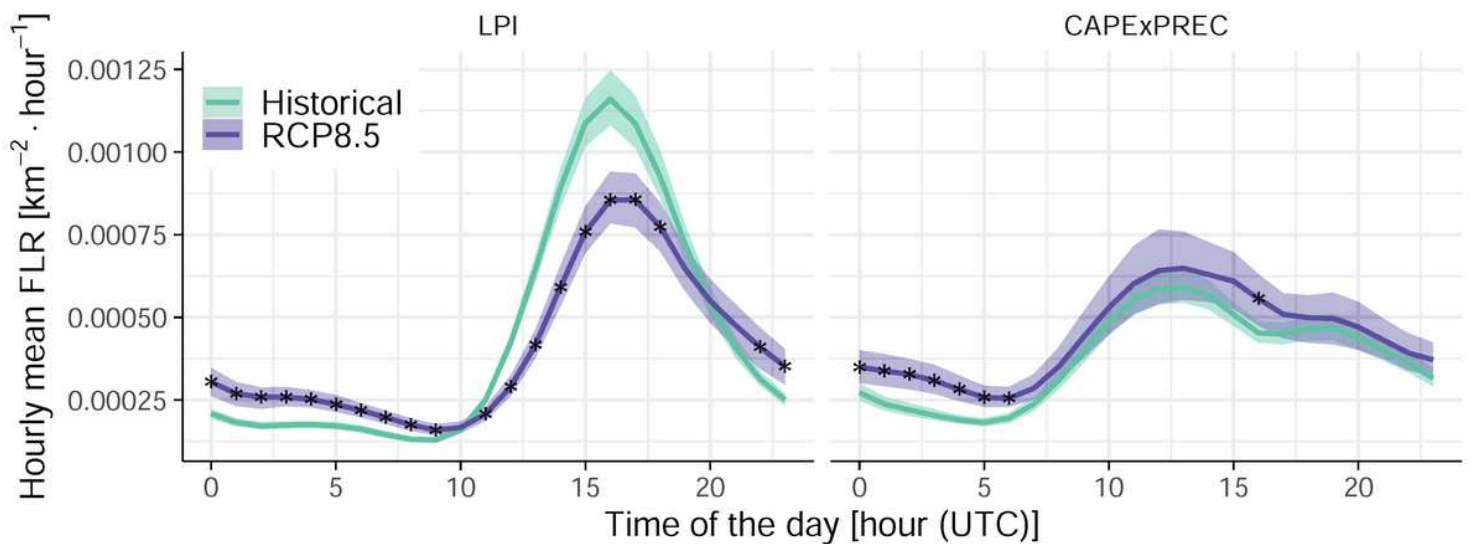


Figure 9

Diurnal cycle of the hourly mean ash rate for the COSMO EC-Earth historical (green) and the EC-Earth future driven simulations (purple). The output of the LPI parameterization is shown on the left, while that of the CAPE \times PREC is shown on the right. The shaded areas indicate the uncertainty derived through the bootstrapping technique with replacement introduced in the method section. Stars indicate hours with a significant change at the 5% level.

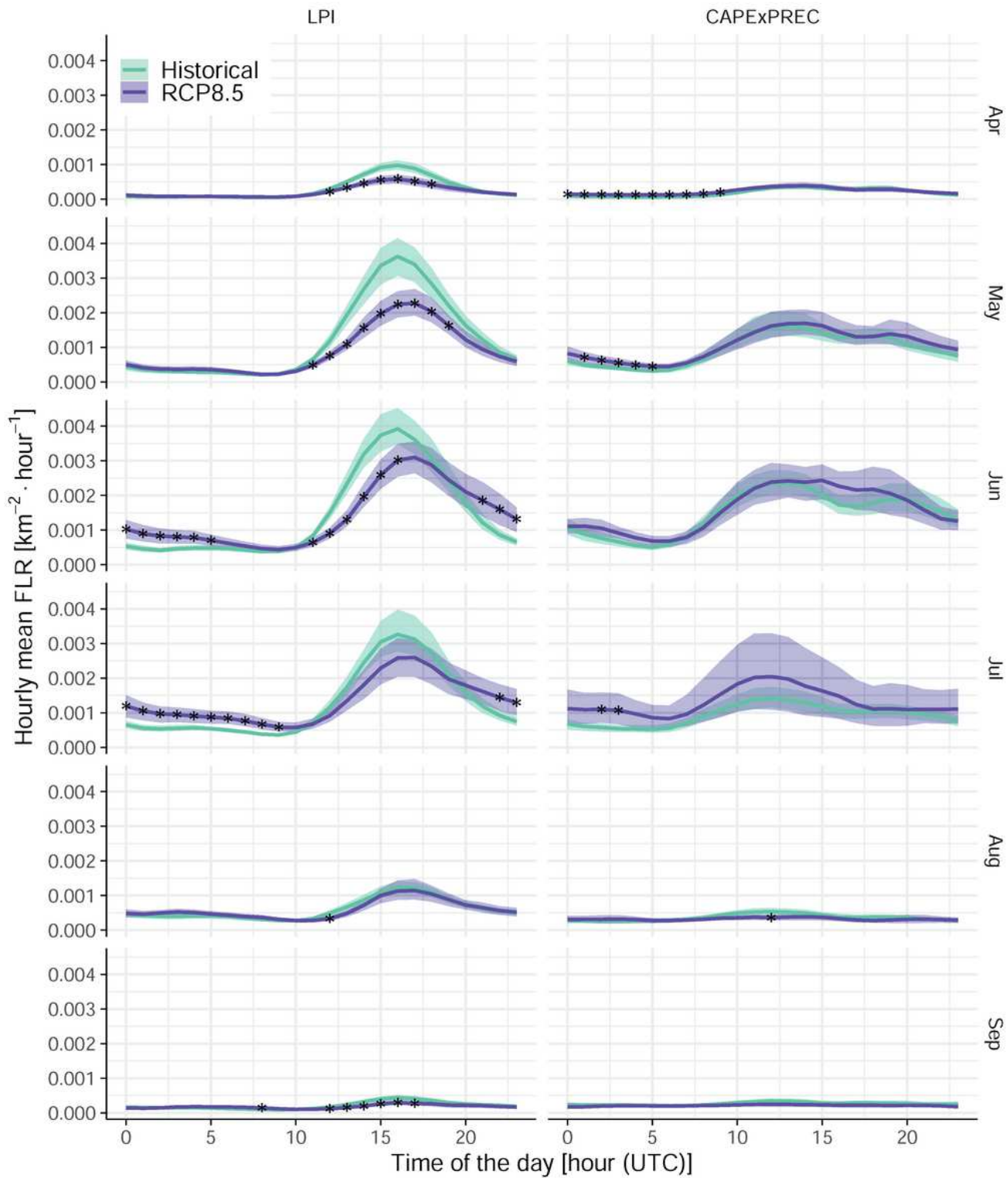


Figure 10

Diurnal cycle of the hourly mean ash rate for the COSMO EC-Earth historical (green) and the EC-Earth future driven simulations (purple). The output of the LPI parameterization is shown on the left, while that of the CAPE \times PREC is shown on the right. Besides, each row shows the diurnal cycle for a given convectively active month (i.e., from April to September). The shaded areas indicate the uncertainty

derived through the bootstrapping technique with replacement introduced in the method section. Stars indicate hours with a significant change at the 5% level.

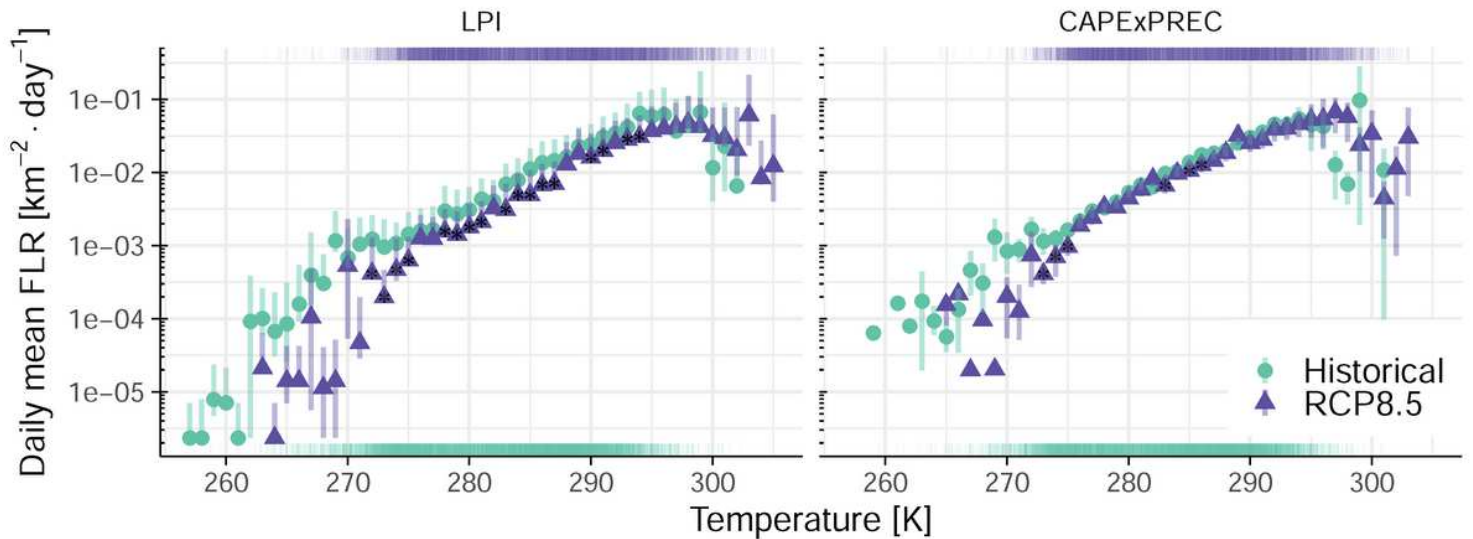


Figure 11

The dependency of the mean daily ash rate with daily mean temperature for the COSMO EC-Earth historical driven simulation (green) and the EC-Earth future driven simulation (purple). The rugs at the bottom and the top of the plot show the occurrence of a given temperature for the corresponding simulation. Flash rates are binned to temperature values (i.e., one point per 1 K). These values are plotted for both the LPI (left column) and the CAPE \times PREC (right column) parameterizations. Stars indicate significant differences between the two simulations at the 5% level. This significance is only indicated for points for which the sample size exceeds 100 days.

Supplementary Files

This is a list of supplementary files associated with this preprint. Click to download.

- [supMatBrissonetalclimDyn20210315.pdf](#)